https://dx.doi.org/10.1016/j.ijmecsci.2023.108625

A Microcracking-based Model for the Dynamic Failure of Carbon/Carbon Composites

Shen Qingliang[1,2*], Yang Guangmeng[3], Xiao Caixiang[2], Song Qiang[2], Li Hejun[2], Yao Xiyuan[2], M.W. Fu[1]

1. Department of Mechanical Engineering, Research Institute for Advanced Manufacturing, The Hong Kong Polytechnic University, Hong Kong, China
2. State Key Laboratory of Solidification Processing, Carbon/Carbon Composites Research Center, Northwestern Polytechnical University, Xi'an 710072, China
3. Jihua Laboratory, Foshan, 528200, China

Abstract:

The 'pseudoplastic' deformation and failure of the carbon/carbon composites (C/Cs) are strain-rate-sensitive while the mechanism has not yet been properly elaborated. To delve into the design and fabrication strategy of the C/Cs towards high strain rate impact applications, the influences of preform architectures and carbon nanotubes (CNT) doping on the dynamic mechanical behaviors of the C/Cs were studied, showing that the CNT-doped plain weave preform exhibits better anti-impact performances than the other structures. The experimental results indicate that the fragmentation of the C/Cs at high strain rate is due to the activation of all the possible cracking paths with excessive kinetic energy deposited, which is significantly different with the growth of a main crack under the quasi-static loading. A two-scale modeling is established to backtrack from the macroscale mechanical response to the microscale cracking behavior, where the quasi-static and dynamic failure of the composite were elaborated within a unified framework of linear elastic fracture mechanism. The coupling of the experiments and modeling revealed that the CNT-doped layer would constrain the microcracking behavior at elevated strain rates. Further nanomechanical tests and molecular dynamics simulations verify that the buffering function and the enhanced energy absorption of the CNT-doped layer are responsible for the improved anti-impact performances of the C/Cs.

Keywords

Carbon-carbon composites (CCCs); CNT doping; Strain rate sensitivity; Deformation and failure.

1. Introduction

Carbon fiber reinforced carbon matrix composites (C/Cs) are excellent thermostructural materials for aerospace applications due to their lightweight, superior thermal stability and mechanical performances up to 3000 °C [1-3]. During the service life of the C/Cs thermal protection parts (i.e., leading edges and heat shields for hypersonic vehicles), they are highly possible to encounter impact loadings [4, 5]. The loss of the space shuttle Columbia was caused by the debris impact and the hole formation in a C/C thermal protection panel, leading to excessive heating and the failure of the left wing integrity [6, 7]. Therefore, understanding,

* Corresponding author. E-mail address: shenqingliang@nwpu.edu.cn (Q.L. Shen)

predicting, and delving into the dynamic fracture of C/Cs are critical for the design of C/C parts towards aerospace applications. However, most of the existing literatures have focused on the quasi-static failure of the C/Cs while the research that concerns with the dynamic failure is rare. The insufficient accumulated knowledge related to the dynamic mechanical behavior and associated damage mechanisms, the high costs involved in both the development and the test of these composites, and the associated intellectual property issues, together make it difficult to achieve an in-depth understanding of the dynamic deformation and failure of the C/Cs.

The dynamic mechanical behavior of C/Cs concerns with both the dynamic deformation at small strains and dynamic failure at large strains. Previous literatures focusing on the dynamic deformation pointed out that the damping of C/Cs are sensitive to the loading strain rates and frequency. Furtherly, the intrinsic matrix and interfacial microcracking were considered as the major source of the damping in the dynamic deformation. The higher defect (interlayer sliding in the matrix and interfacial debonding between the fiber and matrix) density generally results in higher internal friction and more significant damping [8, 9]. Liu et al and Cheng et al also found that the weakening of interfacial strength and matrix microcracking, which is a result of the thermal/mechanical fatigue loadings, would contribute to the increased internal friction of the C/Cs [10-12]. Based on these works, the critical role of microcracking in the dynamic deformation of the C/Cs can be identified.

The dynamic failure of the C/Cs are also found to be strain-rate sensitive. Several literatures have reported that the elevated stiffness, strength, and failure strain with the increased strain rates under different loading conditions [13, 14]. Yuan et al. reported that both the compressive stiffness and strength increased at a strain rate of 500/s compared with the quasi-static loading conditions [15]. Li et al. found that the dynamic strength of the needle punched C/Cs was increased significantly with the strain rate while the brittle fracture feature became more pronounced at higher temperature[16]. Guo et al. also reported that a transformation from nonlinear to brittle failure occurred under the increasing strain rate from 2×10^{-4} to 1862 /s for the needle-punched C/Cs [17]. Furtherly, Jin et al have established an empirical relationship between the dimensionless compressive strength and strain rate for C/Cs by using a bilinear fitting algorithm at different temperatures [14].

Despite that these works successfully proved the strain rate sensitivity of the C/Cs, the intrinsic mechanisms responsible for the strain rate sensitivity has not yet been fully identified, and the role of microcracking was not addressed. As a result, there is still no unified theoretical framework established and no microscale constitutive model proposed to elaborate and predict the failure of the C/Cs at different loading rates. Specifically, it is still difficult to explain the nonlinearity (or 'pseudoplasticity') of the C/Cs which are composited by the brittle carbon fibers (CFs) and pyrolytic carbon (PyC) matrix. Currently, two major challenges exist in establishing a unified theoretical framework dealing with the rate-dependent failure of the C/Cs:

The first challenge is the lack of a microscale constitutive model which could properly describe the fracture of the C/Cs. By far, most of the research works focused on the elastic deformation of the C/Cs [18], while very few efforts were made to model the fracture process.

Additionally, the microstructural features of the C/Cs were always ignored in modeling the fracture of the C/Cs while the macroscale engineering failure criteria was adopted to describe the fracture and post-fracture stiffness degradation. Chao et al. used the Tsai-Wu polynomial criteria and the Puck stiffness degradation coefficient to model the failure and the followed stiffness degradation of the C/Cs under flexural loadings, respectively [19]. Bian et al. simulated the compressive failure of the C/C plates with open holes, where the maximum stress criterion and the von Mises criterion were adopted for the fiber and matrix, respectively [20]. Han et al have utilized a combination of maximum stress and the quadratic nominal stress criterion to predict the mechanical performance of the needle-punched C/Cs [21]. The macroscale dynamic failure of the C/Cs can be thoroughly described and predicted but the microstructural changes cannot be accurately captured or predicted using these models.

The second challenge is how to involve the strain rate sensitivity into the constitutive model. The available rate-dependent constitutive models always proceed within the framework of plasticity. Among them, the Johnson-Cook (J-C) model [22, 23] and the ZWT model [24, 25] are popular. These constitutive models are reasonable in the numerical simulation of metal or polymer materials since the plasticity of polymer and metals have been well recognized and established. On the other hand, the carbon materials are generally regarded as brittle materials, where neither the activation of dislocations nor the stretching/rotating of long chain bonds could be expected for the carbons. There are no experimental evidence supporting or elaborating the physics behind these plasticity-based constitutive models for the C/Cs. However, the plasticity-based constitutive models were utilized in elaborating the rate-dependent behaviors of C/Cs. For example, a strain hardening based constitutive model, which was developed specifically for ductile materials, was used in modeling of the impact failure of the C/C leading edge panels for the Columbia shuttle [26]. In view of this, Guo et al have proposed an analytical model which considers the damage accumulation and the resulted stiffness decrease, where an explicit relationship between the model parameters and the strain rate is established, and it fits well with the macroscale stress-strain curves under both in-plane and out-of-plane compression conditions [13, 27]. However, there is still no available microscale constitutive models that can directly link the microstructural changes (especially the microcracking) to the macroscale dynamic mechanical response of the C/Cs.

Given the brittle nature of the carbon materials, the deformation and failure of the C/Cs should be analyzed within the framework of linear elastic fracture mechanic (LEFM). Among the constitutive models that deal with the dynamic fracture of brittle solids, the phenomenological models (i.e., JH-1, JH-2 and JHB models) are mostly applied due to their computational efficiency and robustness when used for large scale simulations [28-31]. These phenomenological models, however, always require excessive adjustable parameters and suffer from the disadvantages of overfitting. An alternative strategy to establish the constitutive model is to use the continuum damage method. Although it is useful and efficient in defining the deformation and fracture behavior of the composite materials at the macroscale, the microscale details are difficult to be implemented in the continuum damage models. There is still a lack of

efficient modeling strategy to feasibly identify the role of various microstructural modifications and nanomaterial doping on the macroscale mechanical response of a brittle composite. In other words, the current available models cannot answer the most critical problem: how to improve the anti-impact performance of the C/Cs?

From the engineering aspects, the capability to absorb the impact energy of the C/Cs is poor compared with other composites (i.e., metal and polymer matrix composites). It is difficult to improve the anti-impact capability of the C/Cs once the structure of the CF preforms and the properties of the PyC matrix are set. As a result, most of the existing works only focused on the dynamic deformation and failure of C/Cs with a specific preform architecture [4, 5, 14, 15, 17, 32]. In recent years, intensive efforts have been made to the optimization of CF preform, nanomaterial (i.e., carbon nanotubes (CNTs), SiC nanowires, and graphene layers) doping, and many improvements have been achieved in the quasi-static and fatigue performances [33-36]. However, the efficiency of these newly developed modification routines has not yet been evaluated under the dynamic loading conditions. In this research, we demonstrated that the anti-impact performance of the C/Cs can be tailored by varying the CF preform architecture and with the aid of CNT doping. Furthermore, a multiscale modeling framework to connect the microcracking and the macroscale deformation and failure was developed. Three critical problems were addressed: (1) How to incorporate the microcracking into the rate-dependent constitutive model? (2) How does the varied CF preform architecture tailor the fracture behavior at different strain rates? (3) How does the CNT doping influence the microcracking and contribute to the enhanced anti-impact capability?

2. Material and methods

In this section, the details relating to the fabrication, mechanical tests and microstructural characterizations of the C/Cs are provided. In subsection 2.1, the fabrication procedures of the C/Cs with varied preform structures and CNT doping are presented. In subsection 2.2, the quasi-static and dynamic mechanical test details are illustrated, where the essential background knowledge of the Split Hopkinson pressure bar (SHPB) tests are also briefly introduced. In subsection 2.3, the characterizations required for acquiring the multiscale structural features and the nanoindentation behaviors of the C/Cs are given.

2.1 The preparation of the C/Cs with varied preform structures and CNT doping.

Three different types of CF preforms were used, as shown in Fig. 1a-c: (1) the 2.5D needle-punched CF felt (2.5D-C) with a density of 0.60 ± 0.02 g/cm^3; (2) 2D plain-weaved CF laminates (2D-C) with a density of 0.65 ± 0.02 g/cm^3; and (3) CNT doped 2D plain-weaved CF laminates (2D-CNT-C) with a density of 0.66 ± 0.02 g/cm^3. All the preforms are made of the PAN-based CF (T300, Toray Inc). The 2.5D-C was made by the alternate stacking of non-woven CF cloth layer (6K, 0.5 mm in thickness) and short-cut web CF layer (0.5 mm in thickness) followed by the Z-direction needle punch process using the CF yarn (6K). The 2D-C had an ellipse fiber yarn cross-sectional shape which was 0.2 mm in height and 0.8 mm in

width, and the gap between the weaved yarns was 0.2 mm.

The 2D-CNT-C was prepared by the electrophoretic deposition (EPD) of CNTs on CF cloth prior to the stacking of the cloth. The detailed process of the EPD process can be found in Ref. [33]. Briefly, to conduct the EPD of CNTs, CNT powders (Purity: 97%, Diameter: 20-80 nm, Timesnano Inc., China) were dispersed in isopropyl alcohol with a concentration of 1.6 g/L to form the CNT suspension. Subsequently, the CNT suspension solution was ultrasonically dispersed. During the EPD process, the CF cloth (40 mm×60 mm) was fixed as the cathode, and a steel plate with the same size was used as the anode. The EPD time was set as 6 minutes to realize a homogeneous CNT layer on the CF cloth as shown in **Fig. 1d**. After the EPD process, the CNT doped CF cloth was stacked up to form the 2D-CNT-C preform. The volume fractions of the CF and CNT are estimated to be ~36% and 0.5% in the 2D-CNT-C preforms.

All the three types of CF preforms were fully densified by the isothermal chemical vapor infiltration (CVI) method [37], the setup of which is briefly illustrated in **Fig. 1e**. The CVI parameters were set as follows: a total pressure of 5 kPa, deposition temperature of 1000 °C, CH_4 with a flow rate of 20 L/h without dilution gas. The CVI time was 200, 300 and 260 hours for 2.5D-C, 2D-C and 2D-CNT-C, respectively, after which a density of ~1.7 g/cm^3 was achieved for the C/Cs, and the typical microstructures of them are shown in **Fig. 1f-h.** The C/C composites fabricated from the 2.5D-C, 2D-C and 2D-CNT-C preforms are labeled as 2.5D-C/C, 2D-C/C and 2D-CNT-C/C, respectively.

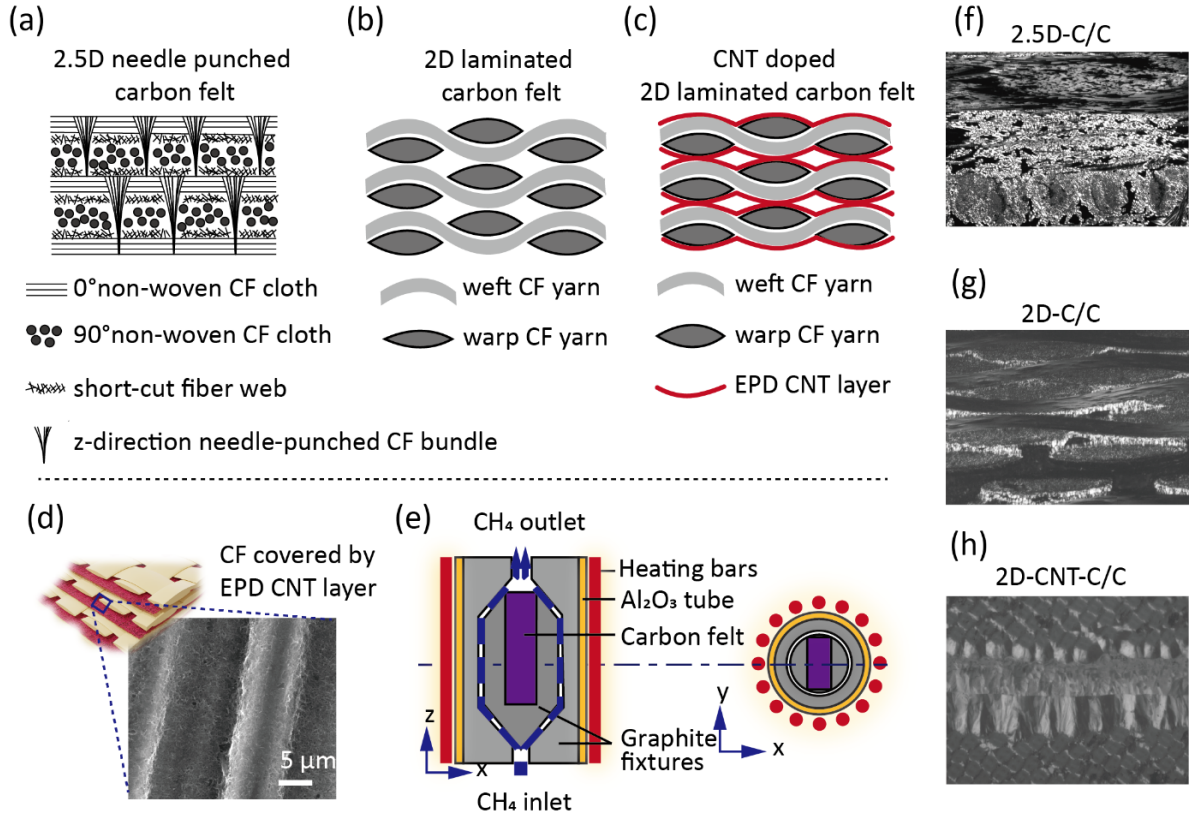

Fig. 1 A brief illustration of the CF preform architectures, CVI densification process and the microstructural of the final 2.5D-C/C, 2D-C/C and 2D-CNT-C/C. (a) the typical structure of the 2.5D needle punched CF felt, which is composed by the stacking of the 0°/90° non-woven

CF cloth and the short-cut CF web, and pinned together by the z-direction needle punched CF bundles. (b) the typical structure of the plain weaved 2D laminated CF felt, which is made by stacking the plain-weaved CF cloth in a uniform direction; (c) the typical structure of the CNT doped plain weaved 2D laminated CF felt, where the CNTs were deposited on the surface of the plain weaved 2D cloth surface via the electrophoretic deposition method; (d) typical morphology of the EPD CNT layer on the CF surface; (e) the setup of the isothermal chemical vapor infiltration of the three types of carbon felts; (f)-(h) the typical polarized light microscope (PLM) photos of the densified 2.5D-C/C, 2D-C/C and 2D-CNT-C/C, where the lighter regions in the micrographs are the infiltrated PyC matrix.

2.2 The setup of the mechanical tests.

The size of the specimens for both the quasi-static and dynamic tests was Φ 5 mm × 3.5 mm, and the heigh was along the layer-stacking direction of the C/Cs. Prior to the mechanical tests, the specimens was polished to a surface roughness lower than 0.5 μm using the diamond paste and ultrasonically cleaned in deionized water. The quasi-static compressive deformation behaviors of the C/Cs were tested using a CMT5304-30KN testing machine at a strain rate of 0.003/s at 28 °C. The force and displacement history of the specimens was recorded by the testing machine. The peak load was adopted to calculate the static compressive strength of the specimen.

The dynamic compressive experiments were conducted using the SHPB apparatus in the strain rates of ~700 - 1800/s as shown in **Fig. 2a**. The strain rates were adjusted by changing the gas pressure of the striker bar. Based on the theory of one-dimensional elastic wave propagation, the stress σ_S, strain ε_S, and strain rate $\dot{\varepsilon}_S$ of the specimen can be evaluated as [38]:

$$\sigma_S = E(\frac{A}{A_S})\varepsilon_T \tag{1}$$

$$\varepsilon_S = -\frac{2C_0}{l_S}\int_0^t \varepsilon_R d\tau \tag{2}$$

$$\dot{\varepsilon}_S = -\frac{2C_0}{l_S}\varepsilon_R \tag{3}$$

$$C_0 = \sqrt{E/\rho_0} \tag{4}$$

where ε_R and ε_T are the transmitted and reflected strain pulses, respectively; C_0 donates the longitudinal elastic wave velocity in the Hopkinson bar; E is Young's modulus of the Hopkinson bars, ρ_0 is the density of the Hopkinson bars; l_s and A_s are the length and cross-sectional area of the specimen; A is the cross-sectional area of the Hopkinson bars. In the current experiments, the striker bar, incident bar and transmission bar were made from the 18Ni-C350 stainless steel (density: 7.8 g/cm^3, yield strength: 300 MPa, Young's modulus: 190 GPa, Poisson's ratio: 0.28, C_0: 5000 m/s). The geometry parameters of the SHPB apparatus are listed in Table 1.

Table 1 The geometry parameters for the SHPB

	Length			Diamater		
SHPB component	Striker Bar	Incident Bar	Transmission Bar	Striker Bar	Incident Bar	Transmission Bar
Valume / mm	200	1200	1200	14.23	14.19	14.20

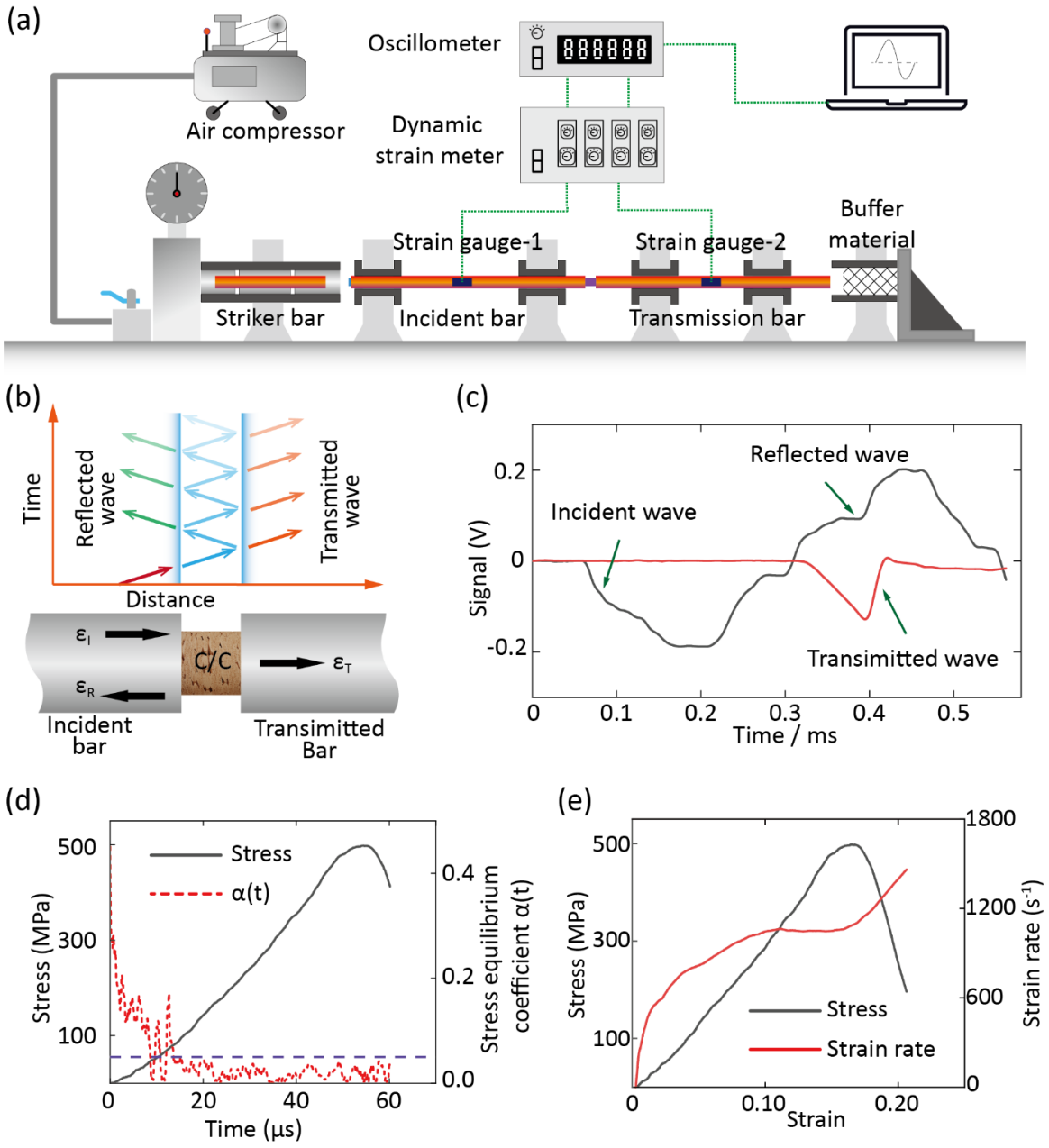

Fig. 2 The setups for the split Hopkinson pressure bar (SHPB) tests: (a) A brief illustration of the SHPB equipment; (b) illustration of the stress wave propagation through the specimen at the SHPB tests; (c) typical signal generated in the dynamic compressive tests using the SHPB tests. (d) the obtained typical experimental stress and stress equilibrium coefficient $\alpha(t)$ vs. time curves, where $\alpha(t)$ is defined by Eqs. 5-7 and is a nondimensional parameter which

measures the difference between the stress on the opposite surface of the specimen; (e) corresponding stress and strain rate vs strain curves -strain of (c).

Two basic assumptions must be satisfied when applying Eqs. 1-3: (1) the one-dimensional stress wave propagation, and (2) stress equilibrium at the opposite surfaces of the specimens in contact with the bars. By using the one-dimensional elastic bars where the duration of the stress pulse employed was much greater than the transit time for the stress pulse in the specimens, assumption (1) was completely considered to meet [39]. Besides, it is imperative to determine whether the stress equilibrium condition is achieved in the specimens during the loading. The stress equilibrium coefficient $\alpha(t)$ is introduced to evaluate the stress equilibrium condition within the specimen [38, 39], and

$$\alpha(t) = \left| \frac{\Delta\sigma(t)}{\sigma_m(t)} \right| \tag{5}$$

$$\Delta\sigma(t) = \sigma(x_1, t) - \sigma(x_2, t) \tag{6}$$

$$\sigma_m(t) = \frac{\sigma(x_1, t) + \sigma(x_2, t)}{2} \tag{7}$$

where $\sigma(x_1, t)$ and $\sigma(x_2, t)$ are stresses on the incident bar/specimen and transmitted bar/specimen interfaces, respectively. A typical $\alpha(t)$ curve of the 2D-C/C is shown in **Fig. 2c**. A dynamic equilibrium deformation state is established after the first 20 μs with the α(t) less than 0.05. At this point, the stress acting on the C/C specimen is about 80 MPa, which is less than 20% of the failure stress. Therefore, the stress equilibrium state was kept for the most part of the impact process (**Fig. 2d**), where the key information related to the stress-strain behavior of the C/Cs could be correctly captured.

Additionally, a copper pulse shaper, 5 mm in diameter and 2 mm in thickness, was used to ensure a constant strain-rate acting on the specimens during the SHPB impact tests [40]. It can be observed from **Fig. 2e** that a quasi-constant strain rate was also achieved with the strain ranging from 0.07 to 0.17, which covered the major deformation stage of the C/Cs. Therefore, both stress equilibrium and constant strain rate were realized in the loading process of the C/Cs during the SHPB test, and the rationality of the experiments can be confirmed. However, a strange rising part of the incident wave signal emerged occasionally when the strain rates were higher than 1200/s (Fig. 2c), which might result from the fracture of the cooper shaper due to its small size. Thus, the match among the shaper diameter, the properties of the bars, the tested specimens and the resulting constant strain rate region should be optimized in future research.

2.3 Characterization details

A nanoindentation system (Hysitron TI980) was used to measure the hardness and indentation modulus of the PyC matrix before and after the CNT doping. Before the indentation tests, the surface of the specimens was polished to a surface roughness less than 0.5 μm. A Berkovich nano-indenter with a tip radius of 20 nm was used, and the maximum load was set as 10 mN with a loading rate of 400 μN/min. The load-displacement curve was extracted from

the indentation tests, and at least five specimens were test for each type of PyC. The damage prior to the final fracture of the specimens was characterized using a micro-Computed Tomography equipment (μ-CT) (Y. Cheetah, Maximum operation voltage: 160 KV; Maximum target power: 10W; 3D resolution: 1.5 μm). The morphologies of the fractured specimens were observed by the scanning electronic microscopy (SEM, GeminiSEM 300, ZEISS). TEM specimens were prepared by ion thinning at a low angle for 5 min (model 691, Gatan). The nanostructure of the CNT doped pyrocarbon was examined by high-resolution transmission electron microscopy (HRTEM, FEI Talos F200X, FEI).

3. The development of a rate-dependent constitutive model for C/Cs based on the linear elastic fracture mechanism (LEFM)

From the aspect of micromechanics, various microcracking processes (i.e., interfacial debonding, fiber breakage, matrix cracking) contribute to the pseudoplasticity of the brittle composites [41], while the collective behavior of the microcracking has not been thoroughly investigated [36, 42-44]. In view of this, an attempt is made to establish a modeling framework which connects the microscale microcracking and the macroscale finite element (FE) modeling under both quasi-static and dynamic loading conditions. The proposed multiscale model is established within the framework of LEFM, the physical foundations of which is more solid than the strain-rate hardening and viscoplasticity for the C/Cs. In addition, the macroscale stress-strain at varied loading rate can be experimentally measured, but the microscale cracking under high strain rates cannot be in-situ monitored and is of more academic interests. Thus, the main goal of the established model is to unravel the evolution tendency of the microcracking behavior in the C/Cs at varied loading rates instead of just simulating the macroscale stress-strain curves. To achieve this goal, the detailed microscale constitutive modeling and macroscale FE modeling are provided in the followed sections, where the strain rate sensitivity is incorporated into the microscale model and the geometrical details of the fiber yarns are simulated in the macroscale model.

3.1 The microscale rate-dependent constitutive model for the C/Cs

In the microscale model, the failure of an element is assumed to be caused by the propagation of multiple microcracks inside the element as shown in **Fig. 3**a. A linear elastic deformation of the element is assumed until the final fracture. The collective microcracking behaviors are addressed in the microscale constitutive model. For the microcracks inside the brittle solids, their evolution generally involves three major processes: (1) the initiation of the microcracks from the existing flaws; (2) the growth of the microcracks under the external loading; (3) the coalescence of the microcracks and the formation of the main crack at the quasi-static loading condition or the fragmentation of the brittle solid at high strain rates.

(1) **The initiation of the microcrack from an existing flaw**

The intrinsic flaws, such as grain boundaries, pores, and misaligned grains, can all possibly cause stress concentrations and serve as the initiation sites of microcracks. Despite that the initiation, growth, and coalescence of multiple microcracks strongly affects the dynamic failure, the detailed evolution (growth and coalescence) of each microcrack is difficult to be tracked in numerical simulations due to the excessive computational costs. Besides, it is also difficult to decide whether a flaw at a specific location would develop into a microcrack or not since various aspects (i.e., the detailed microstructural information around the flaw, temperature, external loading). For simplicity, in the present work it is assumed that the initial microcrack density, η, only relates to the strain rate, and the flaws follow the uniform distribution and orientation in the carbon materials as shown in **Fig. 3a**.

(2) The rate-dependent growth of the microcrack under the external loading

In brittle solids, the growth of the microcracks is driven by local stress concentration at the microcrack tips [45, 46]. The microcracks are assumed to be in the shape of the wing cracks as shown in **Fig. 3**a, where the wing crack is a typical form of microcrack that is commonly used for analyzing the microcrack evolution inside a brittle solid [47]. The wing cracks nucleate from the existing flaws (segment $\mathbf{A_0}$ with a length of $2a$) Under compressive load, frictional sliding over the faces in segmentations $\mathbf{B_1}$ and $\mathbf{B_2}$ is activated, which causes the crack to furtherly grow from the tips. After a short initial curving, $\mathbf{B_1}$ and $\mathbf{B_2}$ will align themselves in the direction to maximize the mode-I stress intensity factor K_I., which is parallel with the maxim principal compression component.

Theoretically, the crack will extend once the stress intensity factor (SIF), K_I, at its tip is higher than the model I critical fracture toughness of the material K_{IC}, or

$$K_I > K_{IC} \tag{8}$$

and the crack extend velocity of the jth crack is defined by [48]:

$$\dot{l}_j = c_{\max}\left(\frac{K_I - K_{IC}}{K_I - 0.5K_{IC}}\right)^{\gamma} \tag{9}$$

where c_{max} is the Rayleigh wave speed of the material and γ is a fitting parameter [49]. The physical meaning of this equation is that: the dynamic growth of the crack is solely determined by the crack tip intensity K_I, while the upper limitation of the crack growth rate is the Rayleigh wave speed c_{max}. Furtherly, according to Sammis and Ashby's work [50], with the applied of only the compressive stress,

$$K_I = \frac{-1.1}{(1+L)^{3.3}}\sigma\sqrt{\pi l} \tag{10}$$

where L is the ratio of the crack length to the flaw radius ($L = l/a$) as shown in **Fig. 3a**.

(3) The collective behavior of the microcracks approaching the final fracture

The most difference between quasi-static and dynamic fracture is that: according to Eq.(9), the velocity at which the microcrack can propagate, $\dot{l}_j$, is finite, at a sufficient high loading rate the coalescence of the microcracks into a main crack is inhibited. Instead, new internal microcracking patterns with much higher density are developed inside the solid to dissipate the

excessive energy deposited in the solids. Thus, in the dynamic fracture, the concept of the main crack is weakened, where the induced microcracks propagate independently until the final fragmentation.

Despite that modulus degradation will occur once the microcracking damage develops inside a brittle solid, the soft stage of the C/Cs from the experimental results is slight in appearance until the final fracture. For reducing the computational costs, a nearly linear microscale constitutive model is proposed for the C/C composite until the damage threshold $f_{threshold}$ is reached, which is followed by the instant fragmentation of the volume without the capability of further load bearing. By setting a uniform damage factor threshold, $f_{threshold}$, the rate-strengthening phenomena can be captured as shown in **Fig. 3c**. In such a way, a rate-dependent linear deformation of the volume V can be defined.

According to the work of Budiansky and O'Connell [51], the damage function $f(t)$ is quantified as:

$$f(t) = \frac{\pi^2}{30}(1+\nu)(5-4\nu)\Omega \tag{11}$$

where ν is the Possion ratio of the material, and Ω is the cracking factor. By assuming that all the wing cracks are of the uniform length and aligned parallel with each other, Ω is defined as:

$$\Omega \equiv \eta l^2 \tag{12}$$

where η is the crack density, l is the length of the wing crack. As demonstrated in **Fig. 3b,** the cracking is activated at a strain of ε_1, and the further increase of the strain enables the propagation of the crack with a speed of $\dot{l}_J$, which is decided by the tip stress intensity factor K_I defined by **Eq. 10**. The failure is defined with a damage threshold $f_{threshold}$, which is decided by both the length of a single crack and the crack density η.

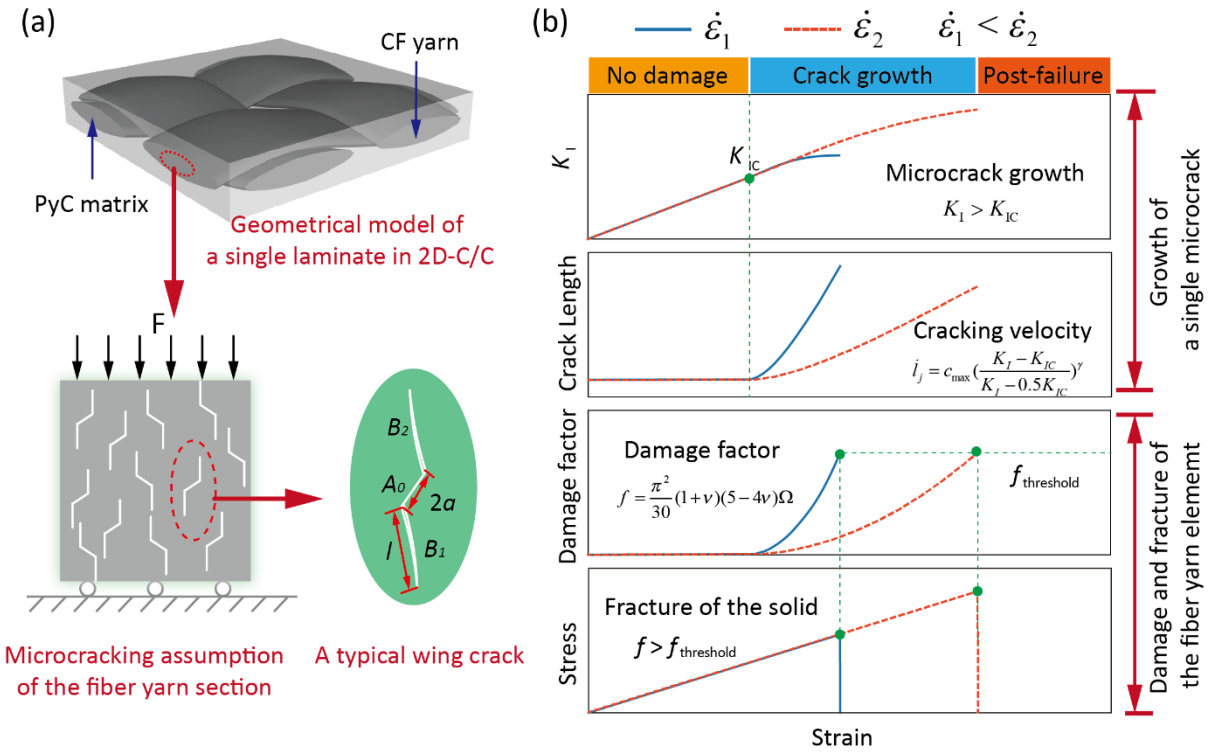

Fig. 3 The microscale RVE constitutive model: (a) The illustration of the basic assumption that there exist a large density of parallel wing cracks within a microscale volume, and the wing crack contains two wings with an initial length l. (b) The illustration of the typical microcrack growth, damage accumulation and fracture process in the constitutive model: (i) A single microcrack will propagate from an initial flaw once the crack tip $K_I > K_{IC}$, and the velocity of microcracking is determined by K_I and limited by c_{max}; (ii) The damage inside one fiber yarn element is determined by the combination of the microcrack density and the wing crack length. When the damage reaches the threshold $f_{threshold}$, an instant fracture of the element is assumed. According to this constitutive model, a higher strain rate (the red dash line) would result in shorter wing crack length and lower damage than the lower strain rate (the blue solid line), which will furtherly contribute to a higher strength under the same $f_{threshold}$.

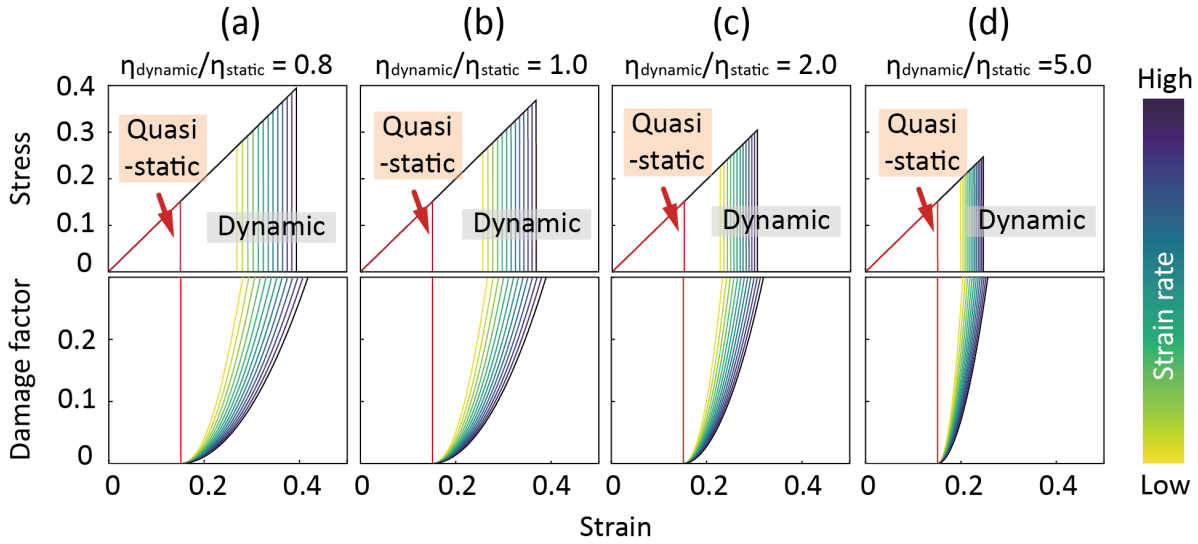

Fig. 4 **The typical stress-strain curves of the microscale elements with different defect density ratio at elevated strain rates** ($\eta_{dynamic}/\eta_{static}$=0.8, 1.0, 2.0 and 5.0 for a-f, respectively), which clearly shows that the $\eta_{dynamic}/\eta_{static}$ can efficiently tailor the dynamic strength of the C/Cs.

Under this basic assumption, the strain rate sensitivity of the brittle elements can be defined as shown in **Fig. 3**b. Among the parameters in the microscale model, the microcracking density η is of primary concern, since it has a significant impact on the failure behavior as shown in **Fig. 4**. It is previous learned that the types and densities of flaws that are triggered to initiate a microcrack are different at different strain rates, thus η is a strain-rate dependent parameter [52]. The optimization of the microstructures will significantly influence the flaw distribution by tailoring the preform structures, porosity, and interfacial bonding states, and a better understanding of the evolution of η with varied preform structures and nanomaterial doping will provide valuable insights for the optimization of the C/Cs.

3.2 The macroscale FE model for simulating the stress-strain response of the C/Cs

The in-situ experimental measurement of the microcracking density at high strain rates is difficult or even impossible. To numerically explore the dynamic microcracking behavior, the microscale constitutive modeling is linked to the macroscale FE modeling. Different microconstituents (CFs, PyC matrix and CNT/PyC interphase) are assembled in the voxel-based macroscale FE model for the 2D-C/C and 2D-CNT-C/C as shown in **Fig. 5a**. The short-cut web layers are involved in the 2.5D-C/C, where the fibers oriented randomly. The microcracking inside the short-cut web layers exhibits more dispersity than in the fiber yarns of the 2D- and 2D-CNT-C/C. As a result, the assumption that all the wing cracks are of the uniform length and orientation is no more valid for the 2.5D-C/C, while the further refine of the constitutive model is beyond the main object of the current work. Therefore, the geometrical model of the 2.5D-C/C has not been involved in the current work and only the experimental

results are provided.

(1) The geometrical modeling of the 2D-C/C and 2D-CNT-C/C

For the 2D-C/C and 2D-CNT-C/C, the voxel-based geometrical modeling at the fiber yarn scale is performed using the TexGen software [53] and reshaped into cylinder shape using a customized python script. The geometry of the yarns is described by a set of sinusoidal curves for a compact contact between the warp and weft yarns. The geometry parameters (*a*: width of the fiber yarn; *l*: the gaps between the fiber yarns; *h:* thickness of the laminate) are measured from the SEM images of the CF cloth. The geometrical model consists of 15 layers of CF cloth, while each layer is consisted by 5 warp and 5 weft yarns. Since only the CFs and PyC matrix can be defined in the original TexGen model, the CNT/PyC interphase was separated from the matrix phase also using another customized python script, where the single layer of matrix voxel neighboring the fiber yarn was defined as the CNT/PyC interphase. The overall size of the unit cell was 1.0 × 1.0 × 0.2 mm^3 for the unit cell as shown in **Fig. 5a**, and the overall size of the tested specimen was Φ 5.0 mm × 3.5 mm. Therefore, enough unit cells were incorporated into the full-scale geometrical models during the FE modeling to accurately simulate the overall mechanical responses. It is then defined that the macroscale mechanical response equals with the averaged mechanical properties of all the voxel elements, where the average stress $\overline{\sigma_{33}}$ and strains $\overline{\varepsilon_{33}}$ in a macroscale model are defined as followed:

$$\overline{\sigma_{33}} = \frac{1}{V}\int_V \sigma_{33} dV \tag{13}$$

$$\overline{\varepsilon_{33}} = \frac{1}{V}\int_V \varepsilon_{33} dV \tag{14}$$

A total of 786000 elements are meshed to account for a more accurate description of the spatial distribution of the microconstituents.

(2) the detailed deformation and failure criteria for the macroscale modeling

To accurately model the geometry features of the microconstituents, generally very large number of voxel elements are required. Thus, the monitoring of the detailed evolution (growth and coalescence) of microcracks within every single voxel element is of extremely high computational costs. To avoid this disadvantage, the followed simplifications are made based on the microscale constitutive model:

(i) **The deformation behaviors of all the voxel elements are assumed to be purely anisotropic elastic** until the final failure and the modulus degradation caused by the microcracking damage is ignored. Specifically, the fiber yarn, PyC matrix and the CNT/PyC interphase in the C/C are modeled with linear orthogonal anisotropic C3D8R elements following the 3D Hooke's law, the stress-strain relationship of them can be expressed as [54]:

$$\begin{Bmatrix}\sigma_1\\ \sigma_2\\ \sigma_3\\ \sigma_4\\ \sigma_5\\ \sigma_6\end{Bmatrix}=\begin{bmatrix}C_{11} & C_{12} & C_{13} & 0 & 0 & 0\\ C_{21} & C_{22} & C_{23} & 0 & 0 & 0\\ C_{31} & C_{32} & C_{33} & 0 & 0 & 0\\ 0 & 0 & 0 & C_{44} & 0 & 0\\ 0 & 0 & 0 & 0 & C_{55} & 0\\ 0 & 0 & 0 & 0 & 0 & C_{55}\end{bmatrix}\begin{Bmatrix}\varepsilon_1\\ \varepsilon_2\\ \varepsilon_3\\ \varepsilon_4\\ \varepsilon_5\\ \varepsilon_6\end{Bmatrix} \tag{15}$$

(ii) **The Gibbs free energy density is adopted as the only failure criteria for the fiber yarn.** Although various failure criteria have been proposed for the composite materials under quasi-static loading conditions [55-58], generally more than 4 or even over 20 parameters are involved in these models. The incorporation of the strain rate will introduce more parameters and further complicate the modeling. From the engineering aspects, there is generally no sufficient experimental data to calibrate these sophisticated models. Additionally, some of the adopted damage parameters cannot be experimentally quantified under the dynamic loading conditions. Thus, in the current situation, the adopted failure criteria should be both simple enough and can bridge the microstructural evolution and the macroscale failure behavior. In view of this, herein the Gibbs free energy density is used here as the failure criteria. The modified Gibbs free energy density, G, is defined as [59, 60]:

$$G=\frac{\sigma_{11}^2}{2E_{11}}+\frac{\sigma_{22}^2}{2E_{22}}+\frac{\sigma_{33}^2}{2E_{33}}+\frac{\tau_{12}^2}{2G_{12}}+\frac{\tau_{13}^2}{2G_{13}}+\frac{\tau_{23}^2}{2G_{23}}-\frac{\nu_{12}\sigma_{11}\sigma_{22}}{E_{11}}-\frac{\nu_{13}\sigma_{11}\sigma_{33}}{E_{11}}-\frac{\nu_{23}\sigma_{22}\sigma_{33}}{E_{22}} \tag{16}$$

In the original expression used by Maimi et al [60], six independent damage parameters are implemented in associated with the stiffness components. However, the stiffness degradation is ignored in the current model, so the use of the damage parameters is avoided. In the simplest form, the element will failure instantly once its Gibbs free energy exceeds the threshold value:

$$G_{in-situ} > G_{threshold} \tag{17}$$

In such a way, only one adjustable parameter $G_{threshold}$ besides the engineering constants is defined, which makes it feasibly to calibrate with the experiments.

The engineering constants of the PyC matrix and the fiber yarn section simulated in our previous research work [61] were used in the current model and listed in Table 2. The modulus of the CNT/PyC interphase was measured using the nanoindentation method, which is shown in the latter section. To model the dynamic fracture of the C/Cs with and without the CNT/PyC interphase, the explicit analysis of the composite model is conducted with a constant strain rate at the top surface and is supported with a fixed rigid body plate at the bottom end as shown in **Fig. 5b**. After the establish of the geometrical model and the definition of the deformation and failure of the voxel elements, the explicit analysis of the impact process was performed as shown in **Fig. 5b**. The proposed failure criteria were implemented into the established model using a customized user subroutine VUMAT. It was assumed that most of the failure during the impact occurred in the fiber yarn section since it owes the highest defect density, the $G_{threshold}$ of the fiber yarn section is set to be the only adjusted parameters. As for the PyC and the

CNT/PyC interphase, large $G_{threshold}$ was adopted to ensure that their fracture was after the fiber yarn section, where a $G_{threshold}$>800 for the PyC and a $G_{threshold}$>2000 for CNT/PyC elements were recommended.

Table 2 The adopted material constants in the macroscale FE modeling

	E_{11} (GPa)	E_{22} (GPa)	E_{33} (GPa)	ν_{12}	ν_{13}	ν_{23}	G_{12} (GPa)	G_{13} (GPa)	G_{23} (GPa)	$G_{threshold}$
CF yarn	143	24	3.5	0.29	0.29	0.27	22	22	4.3	varied
PyC	13	13	3.8	0.29	0.10	0.10	13	13	3	800
CNT/PyC	2.5	2.5	2.5	0.29	0.29	0.29	13	13	3	2000

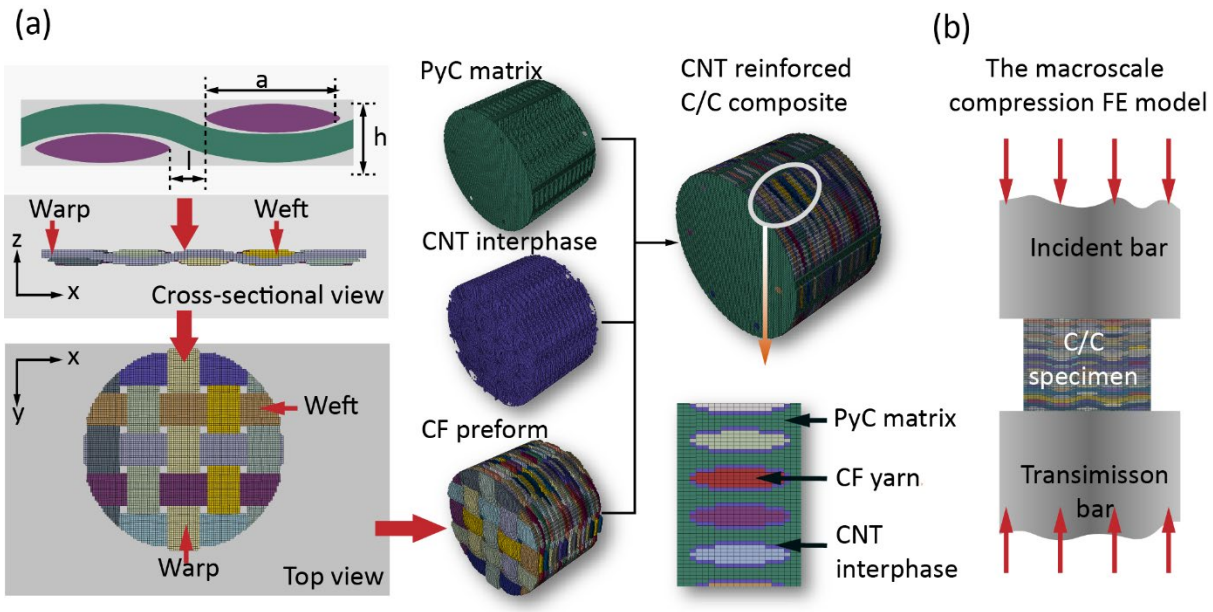

Fig. 5 The macroscale FE model for simulating the stress-strain response of the composite, where (a) a single layer of the plain-weaved fiber cloth is modeled with 5 warp and 5 weft yarns, where *a* is the width of the fiber yarn; *l* is the gap between the fiber yarns; *h* is the thickness of the laminate. The CF preform, CNT interphase and the PyC matrix are assembled to form the whole composite. After the geometrical modeling, the modeled C/C composite is subjected to the compressive stress with designed strain rate, as shown in (b).

3.3 The bridging between the microscale and macroscale models

The gap between the microstructural details and the macroscale dynamic mechanical response is the major challenge for establishing the strain-rate-dependent models for the C/Cs. In view of this, the Gibbs free energy density $G_{threshold}$ adopted in the macroscale modeling is directly related to the microscale cracking behavior. For an element in the microscale constitutive model,

$$G = \int \sigma \, \mathrm{d}\, \varepsilon = G_0(1+\mu(\dot{\varepsilon},\eta)) \tag{18}$$

where G_0 is the Gibbs free energy density under the quasi-static loading condition, and $\mu(\dot{\varepsilon},\eta)$

is the enhancement factor under the dynamic loading. For a purely elastic deformation, once $G_{threshold}$ is acquired, the evolution of the microcracking density at a specific loading rate can be identified by backtracking using the microscale constitutive model. Thus, the Gibbs free energy density G serves as a bridge between the microcracking and the macroscale dynamic failure process as shown in **Fig. 6**. The macroscale geometrical and FE modeling together with the experimental results is to find out the relationship among $G_{threshold}$, $\eta(\dot{\varepsilon})$ and $\dot{\varepsilon}$.

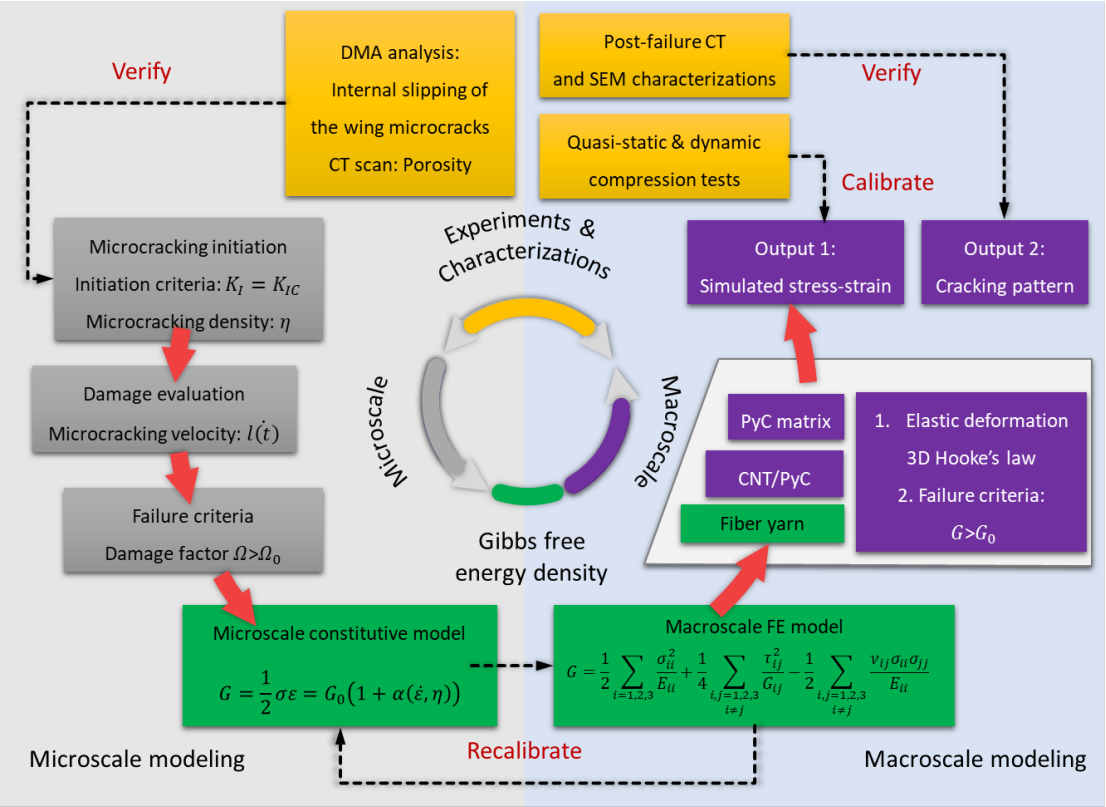

Fig. 6 The connection between the microscale constitutive model and macroscale FE model, where they are bridged by the Gibbs free energy density defined in both the microscale macroscale models. The whole FE modeling is a backtracking process from the macroscale geometrical modelling to the microscale cracking behavior. The experimental results are used to calibrate the stress-strain curve of the macroscale model, and the dynamic mechanical analysis (DMA) and CT characterizations are used to verify the backtracked microscale crack density.

3.4 Molecular Dynamics simulations

Molecular Dynamic simulations were implemented to investigate the effect of CNT doping on the mechanical response of the PyC layers in the nanoscale. All simulations were performed by using the LAMMPS package with the ReaxFF reactive force field specified for hydrocarbons [62]. The size of the simulation box was set as 50×50×50 $Å^3$ and periodic boundary conditions were imposed on X, Y and Z directions. Pure layered Pyrolytic carbon and CNT doped PyC was modeled, respectively. All systems were equilibrated at 300 K for 10

ps to eliminate the irrationality of the initial configuration of the molecules. Afterwards, the systems were heated to the target temperature in 10 ps. OVITO was used to visualize the simulation results [63]. The time step of all simulation was set as 0.25fs.

4. Mechanisms behind the strain rate sensitivity of the C/Cs

The microcracking-based constitutive and geometrical model has been introduced in section 3, and this model will be utilized to unravel the relationships between the microcracking and the macroscale mechanical response of the C/Cs in this section, where the effect of nano-doping on the evolution of the dynamic microcracking density ($\eta(\dot{\varepsilon})$) can be learned. In subsection 4.1 the mechanical testing results at varied $\dot{\varepsilon}$ will be presented. In subsection 4.2, the characterization of the fracture morphologies and the cross validation between the experimental and simulated fracture patterns are performed. In subsection 4.3, the evolution of $\eta(\dot{\varepsilon})$ with $\dot{\varepsilon}$ will be discussed and the influence of nano-doping on $\eta(\dot{\varepsilon})$ will be thoroughly explored. In subsection 4.4, the post-failure fragmentation behaviors of the C/Cs are characterized and the relationship between the ultimate strength and the defects density is obtained.

4.1 The mechanical testing results of the C/Cs at varied loading rates

The strain rate sensitivity of the C/Cs with varied preform structure and CNT doping is experimentally verified in 700 ~1800/s (**Fig. 7**). The stress-strain curves of the 2.5D-C/C indicate the presence of the nonlinearity at a low strain (~20% of the failure strain, **Fig. 7a**), which is caused by the detachment of the needle-punched CF bundles. After this detachment, a quasi-linear deformation is observed until the final fracture. For both the 2D-C/C and 2D-CNT-C/C, linear deformations are confirmed (**Fig. 7 e & i**) with a slight pseudoplasticity stage near the failure, indicating the retained integrity of the specimen during the loading. Both the failure strain and strength of the three types of C/Cs are of statistical scatters, while an overall increasing tendency of the failure stress/strain with the elevated strain rate is detected at ~700-1800 /s. The energy absorption capability E_A prior to the final fracture is also one of the most important capabilities of structural materials. Like the failure strain/stress, the E_A also increased with the strain rate (**Fig. 7**d, h, & l).

An empirical formula is used to fit the dynamic failure strain/strength/E_A with the strain rate $\dot{\varepsilon}$ [64], which is expressed as:

$$F(\dot{\varepsilon}) = F_{\text{static}}(A\log\dot{\varepsilon} + B) \quad \dot{\varepsilon} \in (700,1800) \tag{19}$$

where $F(\dot{\varepsilon})$ stands for the expected failure strain/strength/E_A of the C/Cs varying with $\dot{\varepsilon}$; F_{static} is the compressive failure strain/strength/E_A at the quasi-static condition; the parameters A and B are obtained from the linear regression analysis of the experimental results, where A is the strain rate effect coefficient, and B is the bias coefficient in the linear fitting algorithm. Generally, a higher A indicates a more pronounced strain rate sensitivity.

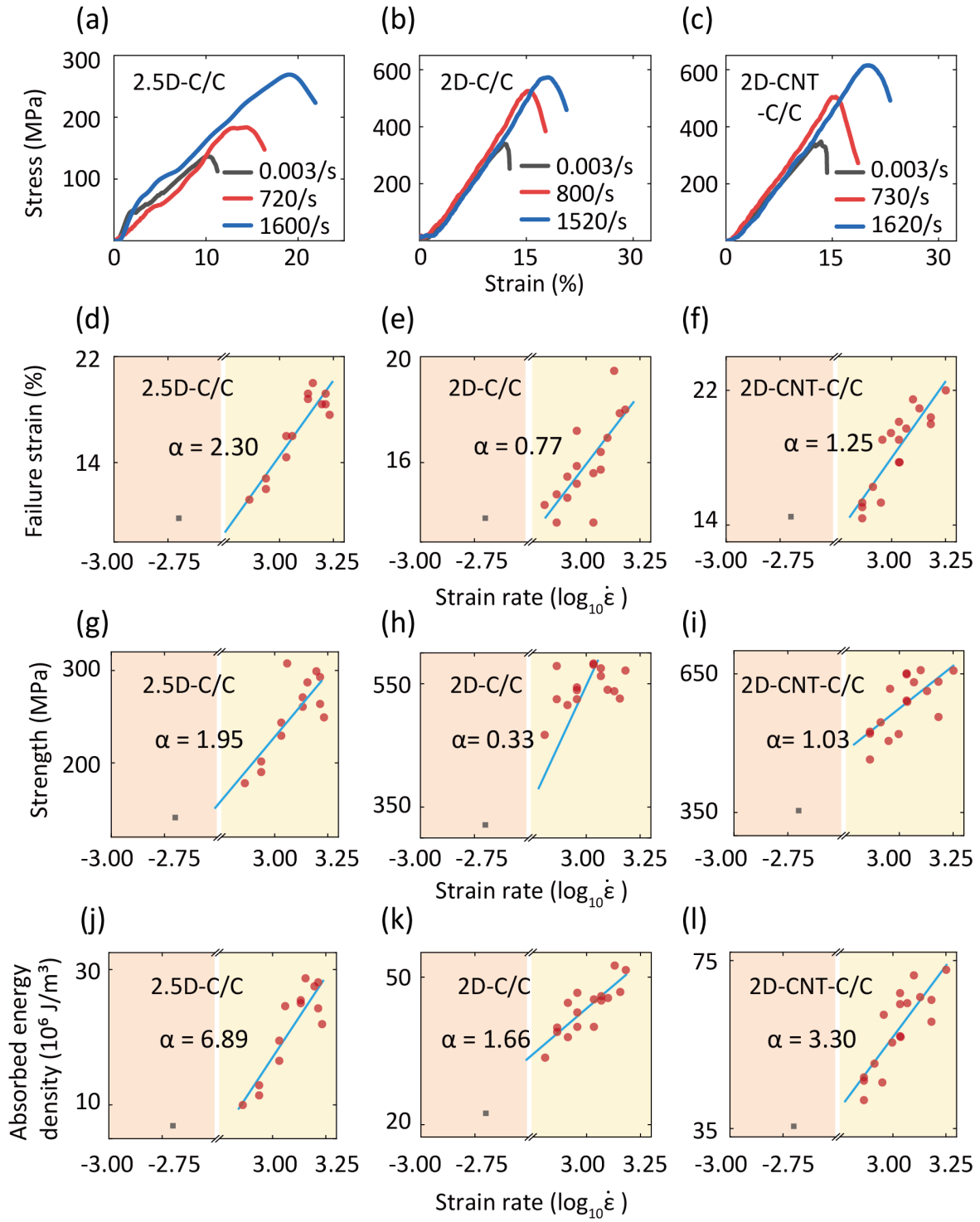

Fig. 7 A summary of the typical mechanical properties of the 2.5D-C/C, 2D-C/C and 2D-CNT-C/C varied with strain rate: (a), (e) and (i) typical stress-strain curves of the 2.5D-C/C, 2D-C/C and 2D-CNT-C/C; (b), (f) and (j) the strain rate vs. failure strain fitting of the 2.5D-C/C, 2D-C/C and 2D-CNT-C/C; (c), (g) and (k) the strain rate vs. strength fitting of the 2.5D-C/C, 2D-C/C and 2D-CNT-C/C; (d), (h) and (l) the strain rate vs. E_A fitting of the 2.5D-C/C, 2D-C/C and 2D-CNT-C/C.

Eq. 19 fits well with all the C/Cs as shown in **Fig. 7**. For the tested specimens, the E_A exhibits the highest A (2.5D-C/C: $A = 6.89$, 2D-C/C: $A = 1.66$, 2D-CNT-C/C: $A = 3.30$) compared with the failure strain (2.5D-C/C: $A = 2.30$, 2D-C/C: $A = 0.77$, 2D-CNT-C/C: $A = 1.25$) and strength (2.5D-C/C: $A = 1.94$, 2D-C/C: $A = 0.37$, 2D-CNT-C/C: $A = 1.03$). Given that the microstructure and mechanical properties of the C/Cs generally exhibit significant scatters [61, 65], the above results indicate that E_A could be a more feasible and profound index for evaluating the strain rate sensitivity than both the failure strain and strength.

A summary of the mechanical results is provided in Fig. 8**a-c**. It is learned from the experiments that: (1) The 2.5D-C/C exhibits the lowest failure strength and E_A under both quasi-static and dynamic loadings (700-1800/s); (2) Compared with the 2.5D-C/C, the 2D-C/C shows the improved anti-impact capability, where the strength and E_A of 2D-C/C improved by 98% and 82%, respectively, compared with the 2.5D-C/C at 100-1800/s; (3) The failure strain and E_A of the 2D-CNT-C/C is improved significantly at 1000-1800/s, but the strength only increases slightly than the 2D-C/C at 1000-1800/s. Compared with the 2.5D-C/C, the failure strain, strength and E_A of 2D-CNT-C/C improve by 8%, 123% and 141%, respectively at 1000-1800/s, clearly demonstrating that the tailoring of the preform structure and CNT doping are efficient in improving the anti-impact capability of the C/Cs. Additionally, compared with the 3D weave-pierced [13], 3D needle-punched [14] and 2.5D needle punched [15] C/Cs, the 2D-CNT-C/C also exhibit superior strength at 700-1000/s. However, currently no available data on the impact behavior of the 3D braided C/Cs has been reported due to their extremely high fabrication costs. Thus, further investigations are still required to provide a more systemic evaluation of the preform structures on the impact behavior of the C/Cs.

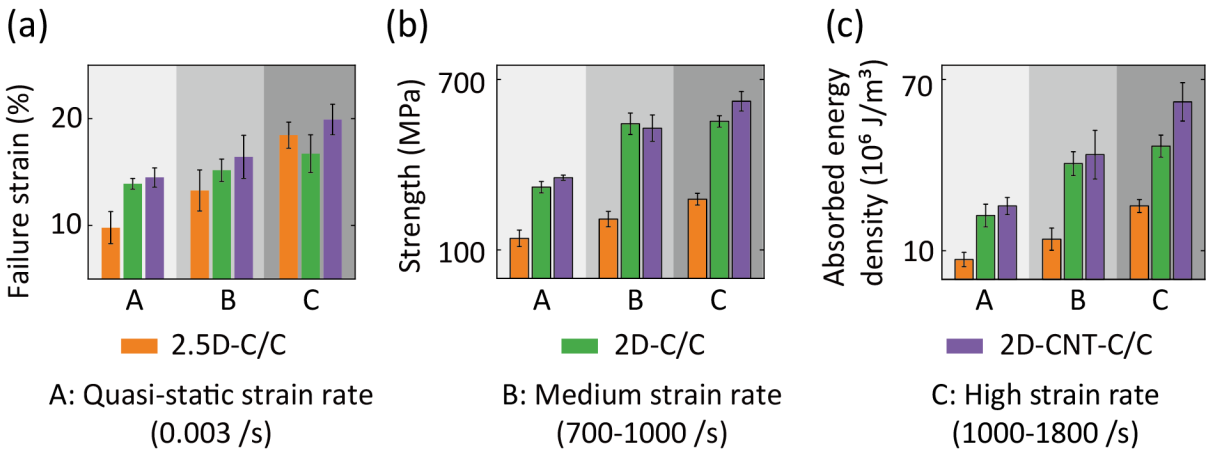

Fig. 8. The average failure strain, strength and E_A of the 2.5D-C/C, 2D-C/C and 2D-CNT-C/C at quasi-static, medium (700-1000 /s) and high (1000-1800 /s) strain rates. (a) The

comparison of the failure strains; (b) the comparison of the strength; (c) The comparison of absorbed energy density.

4.2 The characterization of the fracture morphologies and the simulated cracking pattern

The fracture morphologies of the tested C/Cs under quasi-static loadings are shown in **Fig. 9**. Multiple cracks are observed for all the C/Cs. For the 2.5D-C/C (**Fig. 9a**), the exfoliation of the fiber bundles in Z-direction and the shear cracking inside the short-cut web layers are observed, since the non-woven layers possess superior mechanical strengths than the short-cut web layers. For the 2D-C/C (**Fig. 9**b) and 2D-CNT-C/C (**Fig. 9c**), inter- and intralayer cracks are both observed. This is because that all the layers inside the 2D-C/C and 2D-CNT-C/C are equivalent, so the shear crack would propagate through the layers rather than constrains within a single layer.

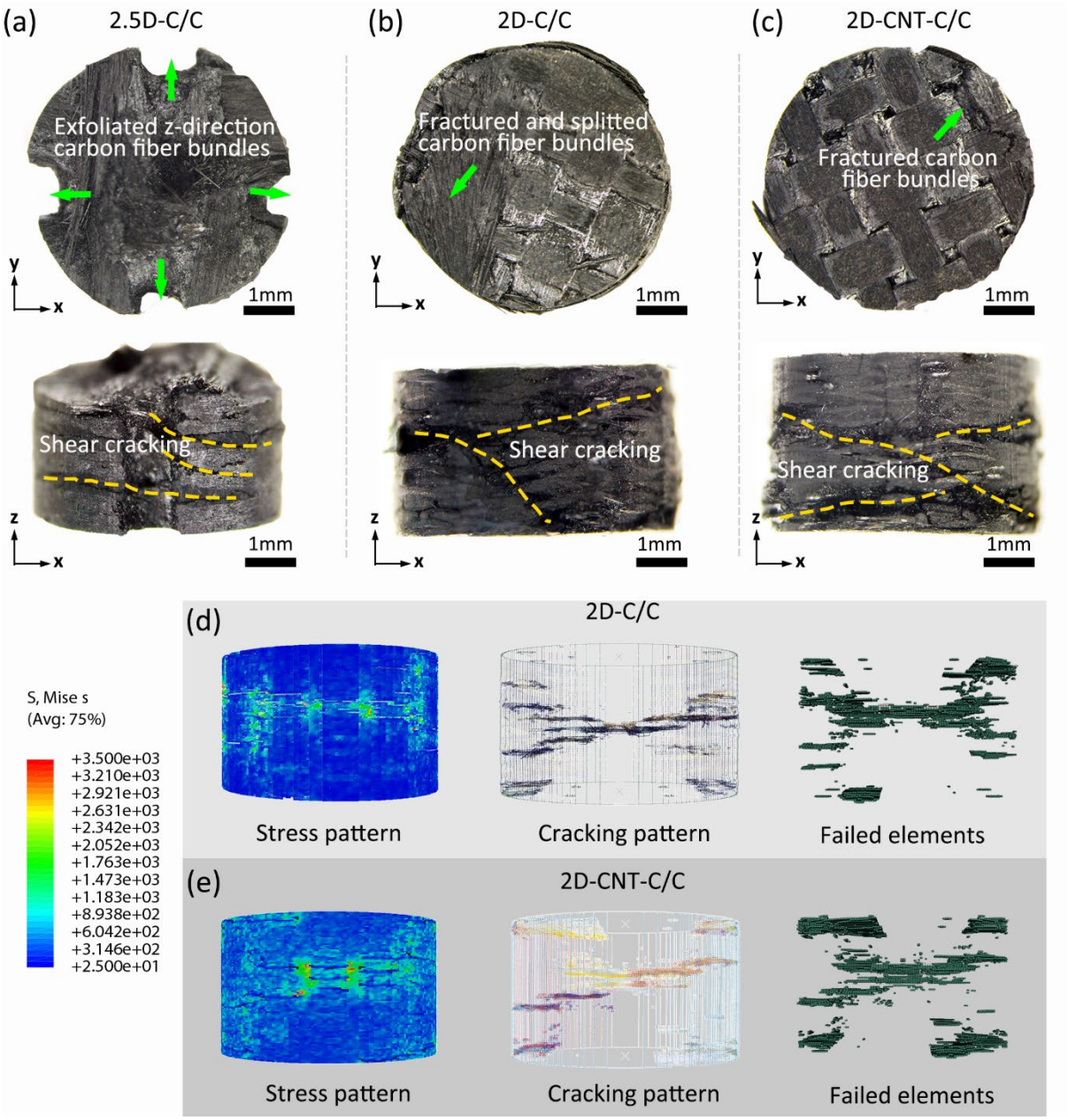

Fig. 9 The experimental and simulated 2.5D-C/C, 2D-C/C and 2D-CNT-C/C cracking patterns under quasi-static compressive loading: (a)-(c) the top and side view of the cracked 2.5D-C/C, 2D-C/C and 2D-CNT-C/C, which are both dominated by the inter- and intralayer shear cracking. (d) and (e) are the simulated cracking pattern of the 2D- and 2D-CNT-C/Cs, where the simulated cracking patterns are consistent with the experimental observations.

On the other hand, the macroscale FE modeling accurately represents both the inter- and intralayer fracture in 2D-C/C and 2D-CNT-C/C (**Fig. 9d&e**). In the simulation process, only the fiber yarn sections are assumed to failure when their in-situ Gibbs energy density, G, excesses the $G_{threshold}$, while the PyC matrix and CNT/PyC interphase are assumed to remain the integrity until the final fracture. The consistency between the experimental observed cracking patterns and the simulated results confirms the rationality of this assumption, which

is also consistent with the fact that the microstructure of the CF yarn sections contains the higher density of flaws (interfaces, microcracks and micropores) than the PyC matrix and the CNT/PyC interphase.

Much higher density of microcracks emerge at elevated strain rates instead of the formation of the main cracks as in the quasi-static tests. The μ-CT images of the SHPB specimens verify this phenomenon (**Fig. 10a, c and e)**. For the 2.5D-C/C at 720 /s, high density microcracks vertical to the layer direction develop in the short-cut web layers (**Fig. 10**a). For the 2D-C/C at 800 /s, several delamination sliding cracks are observed, and slight rotation of the CF yarns also occurs (**Fig. 10**c). On the other hand, for the 2D-CNT-C/C at 730 /s, the interlaminar sliding and torsion of the CF yarns are significantly reduced due to the enhanced interlaminar bonding by the CNT doping ((**Fig. 10**e). Fragmentation of the C/Cs is expected to occur when the strain rate increases furtherly. For the 2.5D-C/C at 1600 /s (**Fig. 10**b), the detaching of the z-direction CF bundles is also detected, while multiple splitting and breakages of the CFs emerge in the short-cut web layer. The collected fragments after the SHPB tests exhibit severe CF bundle breaking/splitting and interfacial debonding. The 2D-C/C at 1520 /s shows multiple fiber bundle breaking accompanied by the debonding of the fibers within the bundle (**Fig. 10**d). Besides, the collected fragments are different from the 2.5D-C/C, where the CF are totally debonded from the PyC matrix and fractured in shorter lengths. After the CNT doping and at 1620 /s, the interfacial debonding inside the remained part is inhibited, but the fragments are in even smaller size, indicating that more CF breakage have occurred, and more energy has been consumed during the impact (**Fig. 10**f).

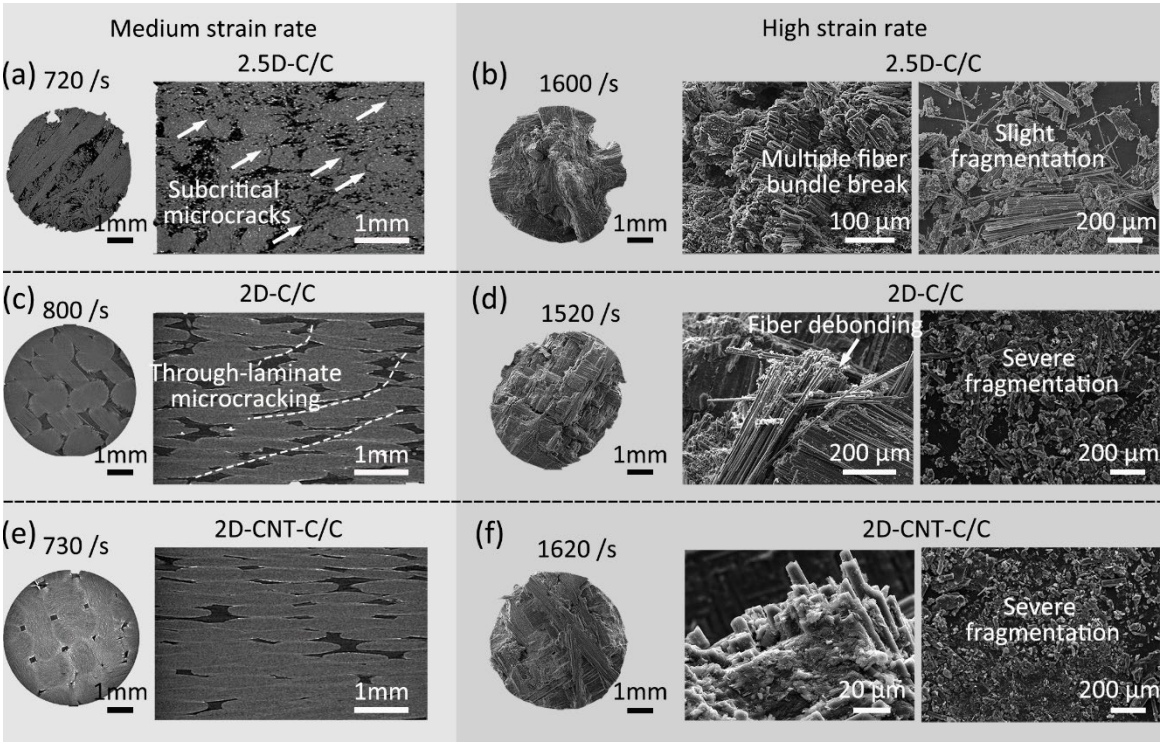

Fig. 10 The fracture morphology of 2.5D-C/C, 2D-C/Cs and 2D-CNT-C/C at the strain rate range of 700-1800 /s characterized by the μ-CT and SEM: (a) the μ-CT slice of the damaged

2.5D-C/C at a strain rate of 720 /s; (b) the fracture morphology of 2.5D-C/C at a strain rate of 1600 /s; (c) the μ-CT slice of the damaged 2D-C/C at a strain rate of 800 /s; (d) the fracture morphology of 2D-C/C at a strain rate of 1520 /s; (e) the μ-CT slice of the damaged 2D-CNT-C/C at a strain rate of 730 /s; (f) the fracture morphology of 2D-CNT-C/C at a strain rate of 1620 /s.

4.3 The microcracking density evolving the strain rate and CNT doping

To better understand the role of CNT doping on the microcracking behavior at high strain rates, the microcracking density $\eta(\dot{\varepsilon})$ is numerically solved based on the multiscale model. The methodology to probe into the microcracking with the aid of the experimental data and the established multiscale modeling is shown in **Fig. 11a.** Since the stress equilibrium is achieved for the tested strain range as discussed in **Section 2**, the $G_{threshold}$ decides the failure stress/strain of the specimen. By tailoring the $G_{threshold}$, continuously evolved stress-strain curves can be obtained, and the $G_{\mathrm{threshold}} - \sigma_{\mathrm{failure}}$ relationship can be determined as shown in **Fig. 11c.** A linear $\sigma_{\mathrm{failure}}$-$\log_{10}(G_{\mathrm{threshold}})$ relationship is captured by the model as shown in **Fig. 11d**. Despite the existence of the CNT/PyC interphase, there is only slight differences between the strength-$\log_{10}(G_{\mathrm{threshold}})$ slope, which is consistent with the experimental results that the doped CNT only contributes to slightly increased strength (**Fig. 7**).

After recalibrating with the experimentally measured strength at varied $\dot{\varepsilon}$, the $\dot{\varepsilon}$ -$G_{\mathrm{threshold}}$ relationship is furtherly identified (**Fig. 11e)**, where a more pronounced increasing tendency of $G_{\mathrm{threshold}}$ with $\dot{\varepsilon}$ is induced after CNT doping. Subsequently, the $G_{\mathrm{threshold}}$-$\dot{\varepsilon}$ relationship is furtherly backtracked using the microscale constitutive model, and thus the $\dot{\varepsilon}$ - $\eta(\dot{\varepsilon})$ relationship can be finally learned. Distinctive cracking behaviors are detected before and after the CNT doping, where the CNT doping significantly restrains the initial $\eta(\dot{\varepsilon})$ and decreases the damage during the impact loading (**Fig. 11f)**. Tehrani et al pointed out that better inter- and intra-laminar strengths by the CNT doping is the reason for the improved anti-impact capacity of the woven CF reinforced carbon nanotube-epoxy composite [66]. However, Bie et al found insignificant increase in the epoxy strength but significantly improved anti-impact performance with CNT doping [67]. The current finding would provide an alternative explanation for this contradictory phenomenon, where the reduces cracking density should be the dominated mechanism contributed to the improved anti-impact performance.

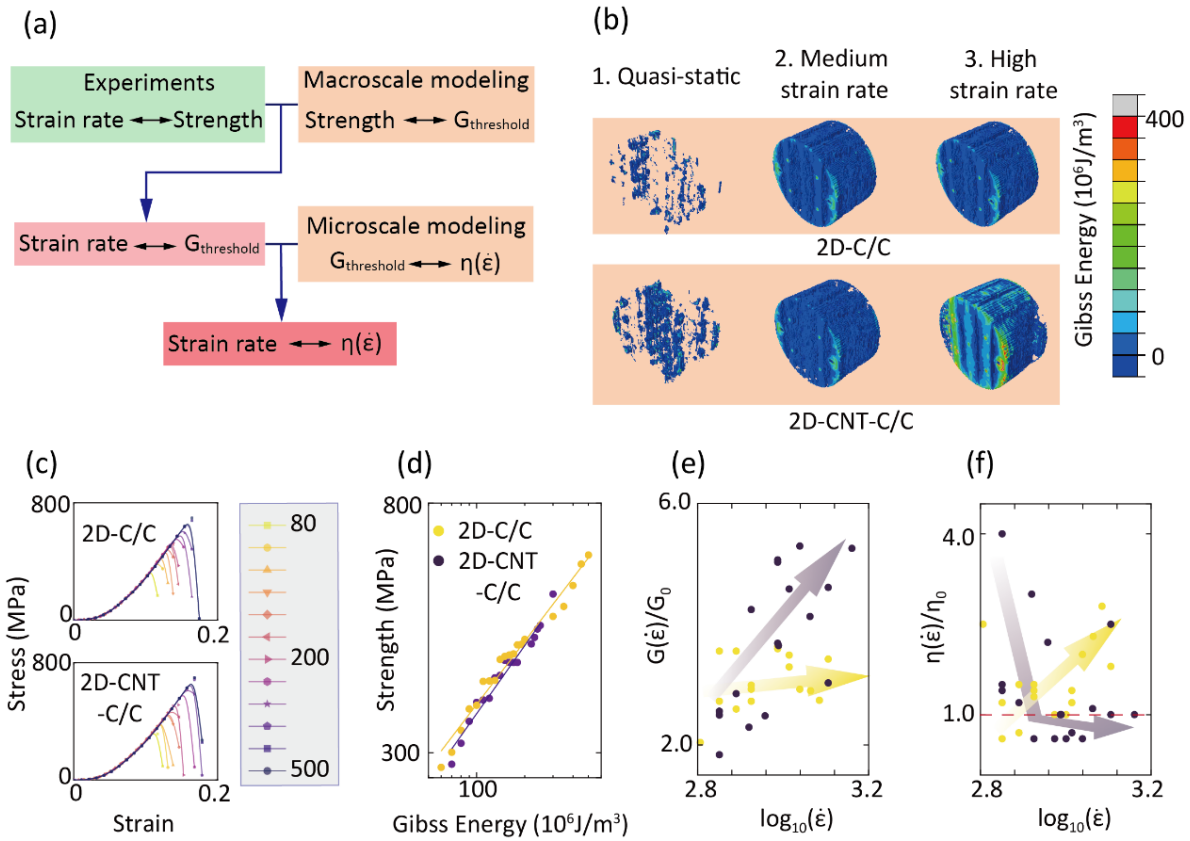

Fig. 11 The simulation results from the microcracking-based constitutive model. (a) the flow chart of the interactions between the experiments and the multiscale model to obtain the $\dot{\varepsilon} - \eta$ relationship. (b) the distribution of the in-situ Gibss free energy density, G, of the 2D- and 2D-CNT-C/C at varied strain rates. Under the quasi-static loading, only a small portion of the elements excesses the $G_{threshold}$ and thus fractures. However, more elements fractures in the 2D-CNT-C/C than in the 2D-C/C. (c) The simulated stress-strain curves of both the 2D- and 2D-CNT-C/C with different $G_{threshold}$; (d) the relationship between the predicted strength and the $G_{threshold}$, showing a linear increase of the strength with the logarithmic increase of the $G_{threshold}$; (e) The calibrated $G_{threshold}$ from the experimental results; (f) The backtracked cracking density at varied strain rates.

4.4 The multiscale fragmentation of C/Cs at varied in-situ free Gibbs energy density

After passing the peak stress, the excessive deposition of kinetic energy would result in fragmentation of the C/Cs, where the excessive $G_{in-situ}$ enables the further growth and multiple bifurcation of the microcracks. As shown in **Fig. 12,** the fragmentation exhibits multiscale features. For the 2D-C/C and 2D-CNT-C/C, in the nanoscale, the layered PyC matrix splits into nanosized debris (**Fig. 12a)**, since the PyC is a typical two-dimensional material with relatively weak interlayer boding. With the decreased $G_{in-situ}$, the nanoscale splitting of the PyC layers is reduced, while the microscale multiple fracture of the CF yarns accompanied by the high-density CF-PyC interface debonding dominants the fragmentation. The further decrease of $G_{in-situ}$ leads to the reduced CF breakage and interfacial debonding density, so the

macroscale debris that retains the assembled yarns can be collected (**Fig. 12d)**. For the 2.5D-C/C, since the CFs are randomly oriented in the short-cut web layer, the multiple fracture of the CF yarns and the shear-induced interface debonding dominants the fragmentation. A significantly lower $G_{in-situ}$ in the 2.5D-C/C is expected due to its low failure strength, and the nanosized splitting of the PyC is not observed. Based on the above observations, it is revealed that the fragmentation in the C/Cs is strongly influenced by the CF yarn orientation and $G_{in-situ}$, where the CF fractures, interfacial debonding and the nanosized splitting of the PyC matrix are the dominant mechanisms of fragmentation.

Additionally, another distinct feature of the dynamic fragmentation is that the crack bifurcations occur in much higher density than in the quasi-static cracking. There is a preference of crack deflection (interfacial debonding) and crack penetration (fiber fracture) when the cracking path encounters the dissimilar interfaces under the quasi-static loading. However, under the dynamic loadings, both the interface debonding and CF breakage have occurred simultaneously at multiple sites. This phenomenon indicates that much more cracking paths are activated upon the deposition of excessive kinetic energy, which is significantly different with the final coalescence of the microcracks into a main crack under quasi-static loading. However, currently the theory of LEFM is still inefficient in dealing with such complex cracking scenarios [68].

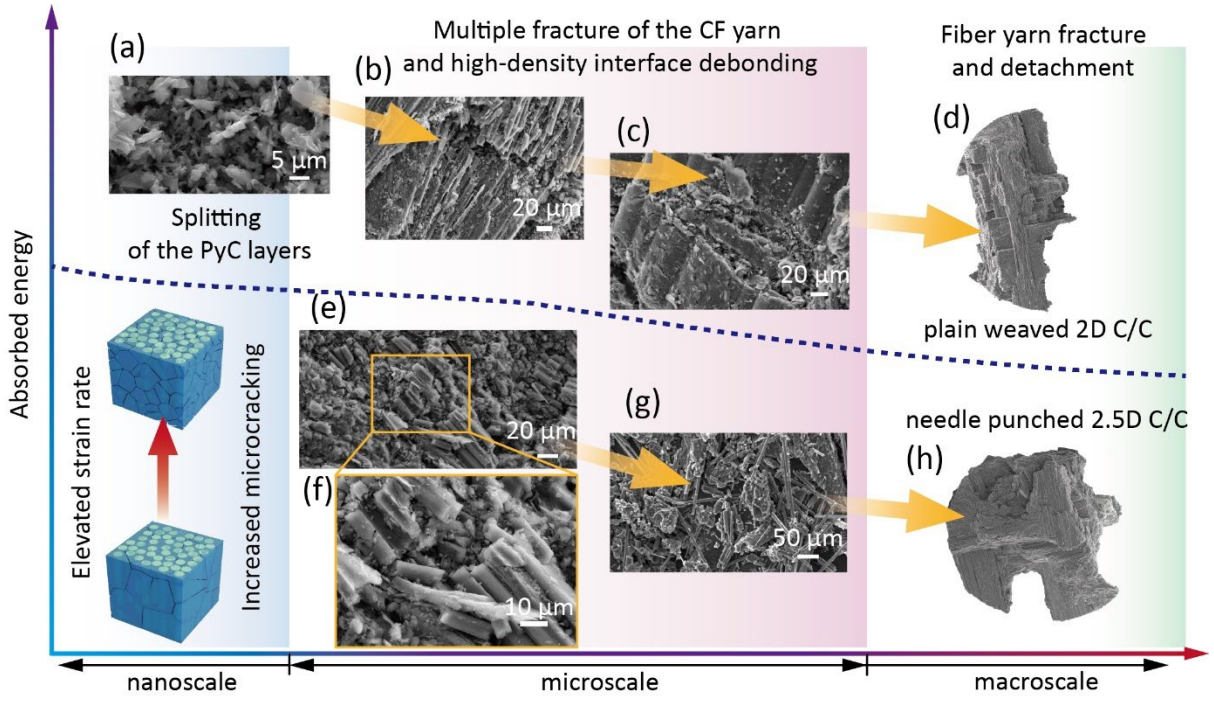

Fig. 12 The fragmentation behavior of plain weaved and needle punched C/C, where the fragmentation of both the 2D-C/C and 2.5D-C/C shows multiscale features. With high absorbed energy, the nano-microscale fragmentation of the matrix is detected for the 2D-C/C. and with the lowered absorbed energy, the multiple fracture of the CFs and the interfacial debonding is detected for both 2D-C/C and 2.5D-C/C. And from the aspect of macroscale observations, the inter- and intralayer microcracking of the fiber cloth are the dominated fragmentation processes.

Meanwhile, it was confirmed in our previous works that the microcracks are efficient in deflecting and bifurcating the main crack, which can help increase the ultimate strength of the C/Cs under quasi-static conditions [36, 61]. Also, the fragmentation behavior (**Fig. 12)** proves that the deterministic role of the main crack in the final fracture is replaced by the individual propagation of all the possible microcracks. This furtherly indicates that the interactions of the microcracks are constrained at higher loading rates, thus a lower density of defects is expected to acquiring better anti-impact strength at high strain rates.

5. The buffering effect of the CNT/PyC layer on the improved anti-impact capability

The above analysis clearly reveals that the tailoring of preform architectures and CNT doping significantly influences the microcracking density in the C/Cs. Furtherly, the role of CNT doping in constraining the microcracking density is discussed as follows.

The pores and the defects inside the PyC matrix are supposed to be the major sources of microcracking of the brittle specimens [69]. During the CVI process, pores are inevitably formed inside the C/Cs, which exhibit significant influence on the microcracking [70]. The porosity of the 2.5D-C/C, 2D-C/C and 2D-CNT-C/C was ~6.8%, 6.5% and 6.2%, respectively (**Fig. 13a&b)**. In all the tested C/Cs, most of the pores are of small size (less than 10^{-3} mm^3, region I&II in **Fig. 13**a). Large pores (region III) can be detected for the 2.5D-C/C but is eliminated in the 2D preforms due to the improved homogeneity of the preform. The portion of medium-sized pores also decreases (10^{-3} to 10^{-1} mm^3, region II in **Fig. 13a**) in the 2D-C/C compared with the 2.5D-C/C. With the doping of CNTs which serve as the nanofillers in the preform, the medium-sized pores in the 2D-CNT-C/C were furtherly reduced. Herein, the reduced porosity induced by the synergy of tailored preform structure and CNT doping would contribute to the weakened stress concentration inside the C/Cs and thus reduced microcracking initiation density.

Internal friction or damping of material refers to the dissipation of energy to the surrounding environment by the reversible microstructural movements, which are mainly composed by the nanoscale relative sliding of the PyC layers and the microscale relative sliding between the CF and the PyC interfaces [71]. Generally, the higher internal friction indicates greater capability to attenuate impact shocks generated during an impact. Two findings are revealed by measuring the internal friction of the C/Cs at the ambient temperature (**Fig. 13c&d)**: (1) the internal friction of the unidirectional C/C is much higher than the 2D-C/C. That is to say, the activated flaws inside the fiber yarn are of much higher density than that in the 2D-C/C, which is consistent with the basic assumption that the CF yarn contains higher intrinsic flaws and thus lower $G_{threshold}$ than the PyC matrix. (2) The internal friction of both the unidirectional C/C and 2D-C/C increases after CNTs doping. Thus, although the CNTs are of low volume fraction, their ability to attenuate the impact shocks are profound.

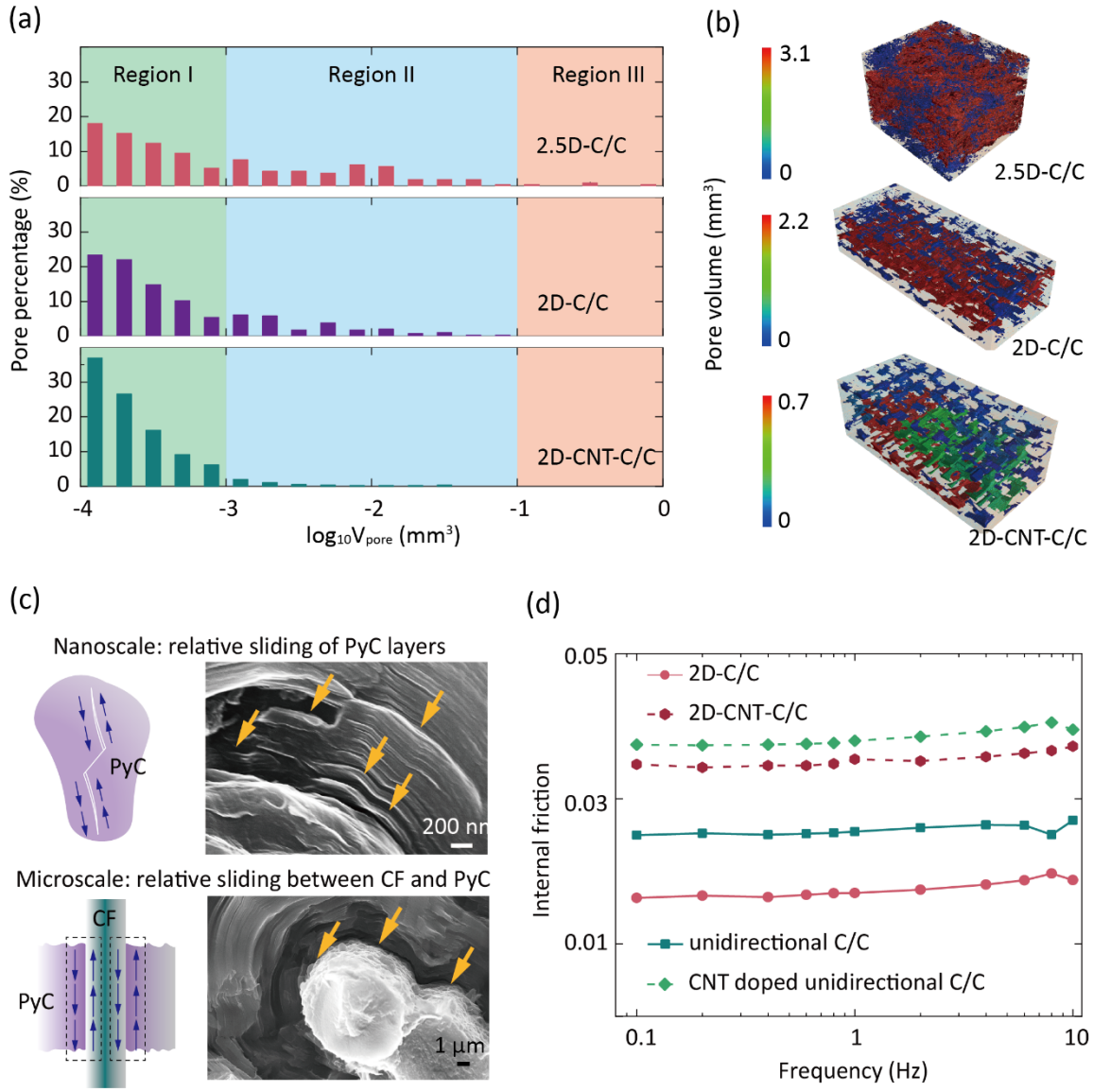

Fig. 13 The characterizations of the possible microstructural defects in the tested C/Cs: (a) the porosity distribution of the 2.5D-C/C, 2D-C/C and 2D-CNT-C/C; (b) the 3D illustrations of the porosity of the 2.5D-C/C, 2D-C/C and 2D-CNT-C/C, respectively. (c) a brief illustration of the sources of internal friction inside the C/Cs, where the nanoscale interlayer friction inside the PyC matrix and the fiber-matrix interfacial sliding are the two dominant mechanisms responsible for the internal friction of the C/Cs. (d) typical internal friction of the unidirectional and 2D C/Cs with and without CNT doping at the frequency of 0.1-10 Hz.

On the other hand, the microstructure of the CNT/PyC interphase is characterized as shown in **Fig. 14**. A homogenous CNT layer is formed on the CF cloth with the aid of the electrophoretic deposition. Then after the CVI process, a dense CNT/PyC interphase can be prepared surrounding the CF (**Fig. 14**b&c). Compared with the original PyC matrix, the CNT doping induces misaligned graphene layers in the CNT/PyC interphase (**Fig. 15**c). As a result, the CNT/PyC layer is much softer than the PyC matrix, which is confirmed by the nanoindentation tests (**Fig. 14** d&e). The indentation modulus of the CNT/PyC layer is only

7.1 GPa, which is only 17.8% of the indentation of PyC matrix (39.6 GPa). Thus, the CNT/PyC interphase serves as a buffer layer, forming the sandwich system together with the PyC matrix and the CFs. Due to the soft nature of the CNT/PyC layer, the impact wave can be significantly attenuated, and the shock energy can be more efficiently absorbed in the 2D-CNT-C/C. On the other hand, the CNT doping does not induce the formation of additional pores inside the C/Cs, and the enhanced internal friction due to the CNT can be ascribed to the misaligned graphene layers (**Fig. 15a-c**). However, from both the fracture (**Fig. 14**b&c) and the analysis in section 3, the flaws induced by the CNT doping has not been activated to initiate microcracks.

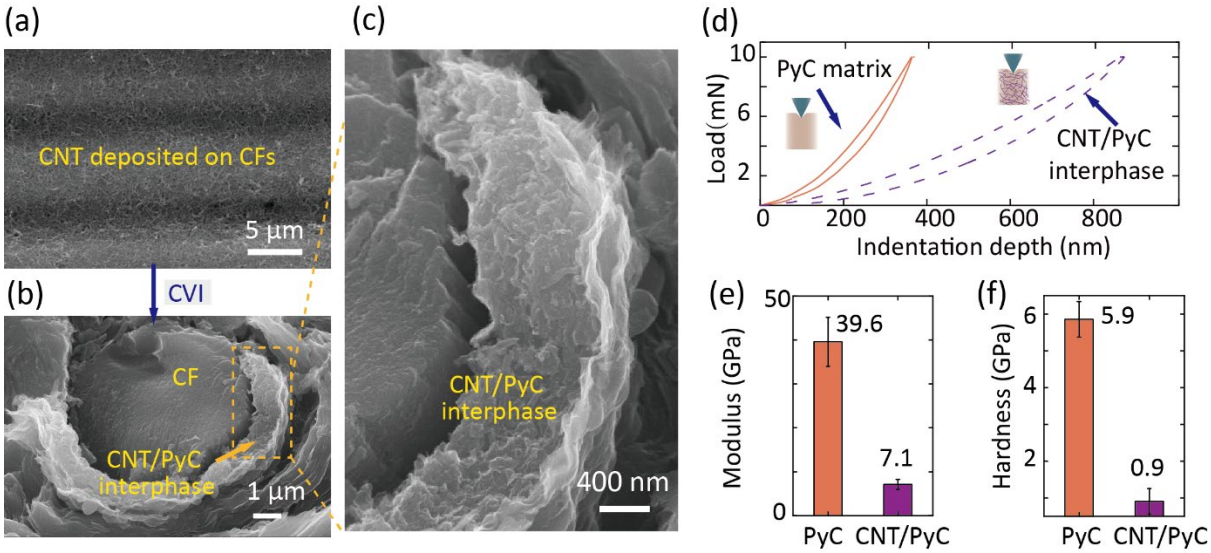

Fig. 14 The construction of the CNT/PyC layers in the 2D-C/C: (a) the morphology of the EPD CNTs on the carbon fiber cloth; (b) the CNT/PyC interphase sandwiches the fiber and the matrix after the CVI process; (c) enlarged SEM morphology of the CNT/PyC layer; (d) typical nanoindentation load-depth curves for the PyC matrix and the CNT/PyC layer; (e) compressive modulus and (f) hardness of the PyC matrix and the CNT/PyC layer, showing that the CNT/PyC layer is much softer than the PyC matrix.

Furtherly, the MD simulation (**Fig. 15**d) confirms that the CNT/PyC layer will failure at a higher stress and thus dissipate more energy upon the compressive loading than the PyC. After CNT doping, the failure stress of the CNT/PyC interphase increases by 36%, with 94.5% more energy dissipated, compared with the original PyC. The unique microstructure of the CNT/PyC interphase contribute to the significantly improved energy absorption capability of the 2D-CNT-C/C. Therefore, the anti-impact capability of the 2D-CNT-C/C can be significantly improved with the buffering function and enhanced energy dissipation of the CNT doping.

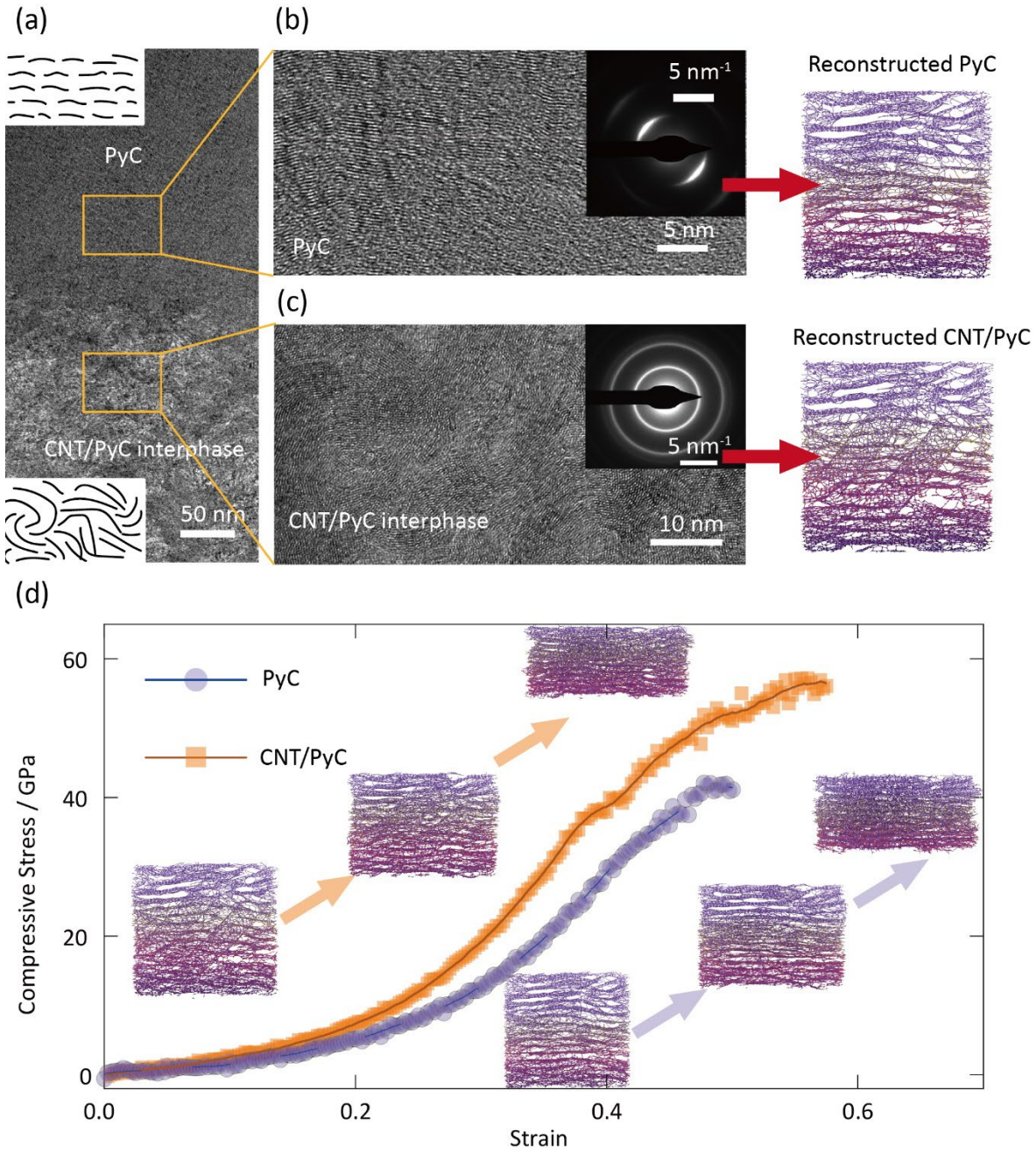

Fig. 15 The comparsions between the microstructural features and nanoscale mecahnical behaviors of the PyC and CNT/PyC. (a) HRTEM image of the interface between the CNT/PyC layer and the CFs; (b) and (c) are the enlarged HRTEM image of the PyC matrix and the CNT/PyC layer with the corresponding selected area electronic diffraction (SEAD) patterns attached at the right-upper area of each HRTEM image. The trips in the HRTEM images are graphene layers, where the stacking manners of the graphene are different in the PyC and CNT/PyC. The selected area electronic diffraction (SEAD) pattern is a statistical result of the preferred orientation of the graphene layers. In the PyC matrix, the graphene layers basically oriented in a uniform direction, where with a preferred orientation angle captured in the SAED pattern. The doping of CNTs into the PyC caused the formation of turbostratic graphene layers. Thus, in the CNT/PyC interphase, the graphene layers were highly curly with unobvious

preferred orientation angle in the related SAED pattern. It can be observed that the PyC was highly anisotropic, but the CNT/PyC interphase showed obvious isotropic features. The right side shows the modeled atomic structures of the PyC and CNT/PyC. (d) MD simulation of the compressive behavior of the simulated stress-strain curve of the CNT/PyC layer and the PyC matrix, the inserted figures are the original and compressed atomic structure of the CNT/PyC layer and the PyC matrix, respectively.

6. Conclusions

In summary, the influences of both the CF preform architectures and CNT doping on the dynamic mechanical behaviors of the C/Cs were experimentally verified and numerically simulated. The experimental results confirmed that the anti-impact capability of the 2D plain-weaved CF preform is better than the 2.5D needle-punched CF preform and could be furtherly improved with CNT doping. The fragmentation of the C/Cs under dynamic loading is mainly consisted by the nanoscale splitting of the PyC matrix, microscale multiple fracture of the CFs accompanied by interfacial debonding, and macroscale fracture/detach of the yarns. This is significantly different with the final coalescence of the microcracks into a main crack under quasi-static loading. The CNT doping enables the construction of CNT/PyC buffer layers, whose modulus is only 17.8% of the PyC matrix. As a result, it could significantly buffers the impact wave and enhance the energy dissipation capability of the C/Cs.

Based on the experimental results, a multiscale modeling strategy was developed to analyze the dynamic fracture of 2D-C/C and 2D-CNT-C/C within the framework of LEFM. The strain rate sensitivity is derived from the collective microcracking behavior at limited velocity, thus both the quasi-static and dynamic failure of the composite can be explained in a unified theoretical framework rather than discussed separately in conventional macroscale models. The model backtracked from the macroscale mechanical response to the microscale cracking behavior and revealed that the CNT/PyC layer would constrain the microcracking behavior at elevated strain rates.

Acknowledgements

This work has been supported by National Natural Science Foundation of China under Grant Nos. 52002322, 52222204, 52293373 and the projects (No. W14V and BBAT) funded by the Hong Kong Polytechnic University.

References

[1] H. Hatta, K. Goto, T. Aoki, Strengths of C/C composites under tensile, shear, and compressive loading: Role of interfacial shear strength, Composites Science and Technology, 65 (2005) 2550-2562.

[2] S. Dietrich, J.-M. Gebert, G. Stasiuk, A. Wanner, K. Weidenmann, O. Deutschmann, I.

Tsukrov, R. Piat, Microstructure characterization of CVI-densified carbon/carbon composites with various fiber distributions, Composites Science and Technology, 72 (2012) 1892-1900.
[3] P. Chowdhury, H. Sehitoglu, R. Rateick, Damage tolerance of carbon-carbon composites in aerospace application, Carbon, 126 (2018) 382-393.
[4] W. Xie, S. Meng, L. Ding, H. Jin, G. Han, L. Wang, F. Scarpa, R. Chi, High velocity impact tests on high temperature carbon-carbon composites, Composites Part B: Engineering, 98 (2016) 30-38.
[5] W. Xie, F. Yang, S. Meng, F. Scarpa, L. Wang, Perforation of needle-punched carbon-carbon composites during high-temperature and high-velocity ballistic impacts, Composite Structures, 245 (2020) 112224.
[6] J.D. Walker, From columbia to discovery: Understanding the impact threat to the space shuttle, International journal of impact engineering, 36 (2009) 303-317.
[7] M.S. Smith, NASA's space shuttle columbia: Synopsis of the report of the columbia accident investigation board, in, 2003.
[8] W. Yang, R.Y. Luo, Z.H. Hou, Y. Zhang, H.D. Shagn, M.Y. Hao, Influence of the microstructure of the carbon matrices on the internal friction behavior of carbon/carbon composites, New Carbon Mater, 31 (2016) 159-166.
[9] X.H. Hou, H.J. Li, J. Shen, C. Wang, Z.G. Zhu, Effects of microstructure on the internal friction of carbon-carbon composites, Mat Sci Eng a-Struct, 286 (2000) 250-256.
[10] Y. Liu, Q.G. Fu, F.L. Zhao, G.D. Sun, H.J. Li, Internal friction vs. thermal shock in C/C composites, Compos Part B-Eng, 106 (2016) 59-65.
[11] J. Cheng, H.J. Li, S.Y. Zhang, L.Z. Xue, W.F. Luo, Internal friction behavior of unidirectional carbon/carbon composites after different fatigue cycles, Mat Sci Eng a-Struct, 600 (2014) 129-134.
[12] Q.L. Shen, Q. Song, H.J. Li, C.X. Xiao, T.Y. Wang, H.J. Lin, W. Li, Fatigue strengthening of carbon/carbon composites modified with carbon nanotubes and silicon carbide nanowires, International Journal of Fatigue, 124 (2019) 411-421.
[13] F. Guo, Q.G. Fei, Y.B. Li, N. Gupta, Dynamic Out-of-Plane Compressive Failure Mechanism of Carbon/Carbon Composite: Strain Rate Effect on the Defect Propagation and

Microstructure Failure, J Eng Mater-T Asme, 143 (2021).

[14] X. Jin, C. Hou, C. Li, X. Wang, X. Fan, Strain rate effect on mechanical properties of 3D needle-punched C/C composites at different temperatures, Composites Part B: Engineering, 160 (2019) 140-146.

[15] Y. Qinlu, L. Yulong, L. Hejun, L. Shuping, G. Lingjun, Quasi-static and dynamic compressive fracture behavior of carbon/carbon composites, Carbon, 46 (2008) 699-703.

[16] D.-s. Li, H.-W. Duan, W. Wang, D.-y. Ge, L. Jiang, Q.-q. Yao, Strain rate and temperature effect on mechanical properties and failure of 3D needle-punched Carbon/Carbon composites under dynamic loading, Composite Structures, 172 (2017) 229-241.

[17] F. Guo, Q. Fei, P. Zhang, Y. Li, M. Wang, N. Gupta, Dynamic shear fracture behaviors and "pseudo-plastic" constitutive model of carbon/carbon composite pins, International Journal of Mechanical Sciences, 187 (2020) 105903.

[18] Y.J. Xu, P. Zhang, H. Lu, W.H. Zhang, Hierarchically modeling the elastic properties of 2D needled carbon/carbon composites, Composite Structures, 133 (2015) 148-156.

[19] X.J. Chao, L.H. Qi, W.L. Tian, X.H. Hou, W.J. Ma, H.J. Li, Numerical evaluation of the influence of porosity on bending properties of 2D carbon/carbon composites, Compos Part B-Eng, 136 (2018) 72-80.

[20] T.Y. Bian, Z.D. Guan, F.Q. Liu, Compressive experiment and numerical simulation of 3D carbon/carbon composite open-hole plates, Arch Appl Mech, 88 (2018) 913-932.

[21] M. Han, C.W. Zhou, H.J. Zhang, A mesoscale beam-spring combined mechanical model of needle-punched carbon/carbon composite, Composites Science and Technology, 168 (2018) 371-380.

[22] X. Wang, C. Huang, B. Zou, H. Liu, H. Zhu, J. Wang, Dynamic behavior and a modified Johnson–Cook constitutive model of Inconel 718 at high strain rate and elevated temperature, Materials Science and Engineering: A, 580 (2013) 385-390.

[23] G.R. Johnson, A constitutive model and data for materials subjected to large strains, high strain rates, and high temperatures, Proc. 7th Inf. Sympo. Ballistics, (1983) 541-547.

[24] M. Xu, L. Wang, A new method for studying the dynamic response and damage evolution of polymers at high strain rates, Mechanics of Materials, 38 (2006) 68-75.

[25] X. Xu, S. Gao, D. Zhang, S. Niu, L. Jin, Z. Ou, Mechanical behavior of liquid nitrile rubber-modified epoxy resin: experiments, constitutive model and application, International Journal of Mechanical Sciences, 151 (2019) 46-60.

[26] K. Gwinn, K. Metzinger, Analyses of Foam Impact onto the Columbia Shuttle Wing Leading Edge Panels Using Pronto3d/SPH, in: 42nd AIAA Aerospace Sciences Meeting and Exhibit, 2004, pp. 942.

[27] R. Larsson, V. Singh, R. Olsson, E. Marklund, A micromechanically based model for dynamic damage evolution in unidirectional composites, International Journal of Solids and Structures, 238 (2022).

[28] M.R.I. Islam, J. Zheng, R.C. Batra, Ballistic performance of ceramic and ceramic-metal composite plates with JH1, JH2 and JHB material models, International Journal of Impact Engineering, 137 (2020) 103469.

[29] G. Johnson, T. Holmquist, A computational constitutive model for brittle materials subjected to large strains, high strain rates and high pressures, Shock wave and high-strain-rate phenomena in materials, (1992) 1075-1081.

[30] G.R. Johnson, T.J. Holmquist, An improved computational constitutive model for brittle materials, in: AIP conference proceedings, American Institute of Physics, 1994, pp. 981-984.

[31] G.R. Johnson, T.J. Holmquist, S.R. Beissel, Response of aluminum nitride (including a phase change) to large strains, high strain rates, and high pressures, Journal of Applied Physics, 94 (2003) 1639-1646.

[32] F. Guo, Q. Fei, Y. Li, N. Gupta, Strain-Rate-Dependent In-Plane Compressive Properties of 3D Fine Weave Pierced C/C Composite: Failure Mechanism and Constitutive Model, Acta Mechanica Solida Sinica, 35 (2022) 63-78.

[33] Q. Shen, H. Li, W. Li, Q. Song, Realizing the synergy of carbon nanotubes and matrix microstructure for improved flexural behavior of laminated carbon/carbon composites, Journal of Alloys and Compounds, 738 (2018) 49-55.

[34] L. Han, Q. Song, J. Sun, K. Li, Y. Lu, The role of CNT in improving the mechanical strength retention rate of C/C composites during heat treatment, Composites Part B: Engineering, 187 (2020) 107856.

[35] T. Wang, H. Li, Q. Shen, K. Li, W. Li, Q. Song, S. Zhang, Dependence of mechanical properties on microstructure of high-textured pyrocarbon prepared via isothermal and thermal gradient chemical vapor infiltration, Composites Part B: Engineering, 192 (2020) 107982.

[36] Q. Shen, Q. Song, H. Li, C. Xiao, T. Wang, H. Lin, W. Li, Fatigue strengthening of carbon/carbon composites modified with carbon nanotubes and silicon carbide nanowires, International Journal of Fatigue, 124 (2019) 411-421.

[37] W. Zhang, Z. Hu, K. Hüttinger, Chemical vapor infiltration of carbon fiber felt: optimization of densification and carbon microstructure, Carbon, 40 (2002) 2529-2545.

[38] Y. Wang, Y. Li, T. Suo, X. Luan, D. Zhou, S.M. Zakir, C. Chen, H. Liu, Y. Duan, In-plane mechanical behavior and failure mode of a 2D-SiC/SiC composite under uniaxial dynamic compression, Ceramics International, 44 (2018) 20058-20068.

[39] G. Ravichandran, G. Subhash, Critical appraisal of limiting strain rates for compression testing of ceramics in a split Hopkinson pressure bar, J Am Ceram Soc, 77 (1994) 263-267.

[40] C. Zhang, T. Ren, X. Zhang, W. Hu, Z. Wang, B. Wang, T. Suo, Study of dynamic compressive behaviors of 2D C/SiC composites at elevated temperatures based on in-situ observation, Journal of the European Ceramic Society, 40 (2020) 5103-5119.

[41] V.I. Levitas, Phase transformations, fracture, and other structural changes in inelastic materials, International Journal of Plasticity, 140 (2021) 102914.

[42] J. Kimberley, K. Ramesh, N. Daphalapurkar, A scaling law for the dynamic strength of brittle solids, Acta Materialia, 61 (2013) 3509-3521.

[43] J. Cheng, H.-j. Li, S.-y. Zhang, L.-z. Xue, Effect of matrix sub-layer interfacial fracture on residual strength improvement of the fatigued carbon/carbon composites, Journal of materials science & technology, 34 (2018) 1243-1249.

[44] J. Zhang, W. Liu, Q. Zhu, J. Shao, A novel elastic–plastic damage model for rock materials considering micro-structural degradation due to cyclic fatigue, International Journal of Plasticity, (2022) 103496.

[45] R.L. Kranz, Microcracks in rocks: a review, Tectonophysics, 100 (1983) 449-480.

[46] H.S. Bhat, A.J. Rosakis, C.G. Sammis, A micromechanics based constitutive model for brittle failure at high strain rates, Journal of Applied Mechanics, 79 (2012).

[47] M.F. Ashby, amp, S. Hallam, The failure of brittle solids containing small cracks under compressive stress states, Acta metallurgica, 34 (1986) 497-510.

[48] B. Paliwal, K. Ramesh, An interacting micro-crack damage model for failure of brittle materials under compression, Journal of the Mechanics and Physics of Solids, 56 (2008) 896-923.

[49] C. Katcoff, L. Graham-Brady, Modeling dynamic brittle behavior of materials with circular flaws or pores, International Journal of Solids and Structures, 51 (2014) 754-766.

[50] C. Sammis, M. Ashby, The failure of brittle porous solids under compressive stress states, Acta metallurgica, 34 (1986) 511-526.

[51] B. Budiansky, R.J. O'connell, Elastic moduli of a cracked solid, International journal of Solids and structures, 12 (1976) 81-97.

[52] K. Ramesh, J.D. Hogan, J. Kimberley, A. Stickle, A review of mechanisms and models for dynamic failure, strength, and fragmentation, Planetary and Space Science, 107 (2015) 10-23.

[53] H. Lin, L.P. Brown, A.C. Long, Modelling and simulating textile structures using TexGen, in: Advanced Materials Research, Trans Tech Publ, 2011, pp. 44-47.

[54] E.J. Barbero, Finite element analysis of composite materials using AbaqusTM, CRC press Boca Raton, 2013.

[55] J. Echaabi, F. Trochu, R. Gauvin, Review of failure criteria of fibrous composite materials, Polymer composites, 17 (1996) 786-798.

[56] Z. Hashin, Fatigue failure criteria for unidirectional fiber composites, (1981).

[57] F. Paris, K.E. Jackson, A study of failure criteria of fibrous composite materials, in, 2001.

[58] C.-S. Lee, J.-H. Kim, S.-k. Kim, D.-M. Ryu, J.-M. Lee, Initial and progressive failure analyses for composite laminates using Puck failure criterion and damage-coupled finite element method, Composite Structures, 121 (2015) 406-419.

[59] C. Lopes, P. Camanho, Z. Gürdal, P. Maimí, E. González, Low-velocity impact damage on dispersed stacking sequence laminates. Part II: Numerical simulations, Composites Science and Technology, 69 (2009) 937-947.

[60] P. Maimí, P.P. Camanho, J. Mayugo, C. Dávila, A continuum damage model for composite laminates: Part I–Constitutive model, Mechanics of materials, 39 (2007) 897-908.

[61] S. Qingliang, Y. Guangmeng, X. Caixiang, L. Hejun, S. Qiang, L. Jinhua, M. Fu, Control of multi-scale cracking for improvement of the reliability of carbon/carbon composites via design of interlaminar stress, Composite Structures, 297 (2022) 115985.

[62] A.P. Thompson, H.M. Aktulga, R. Berger, D.S. Bolintineanu, W.M. Brown, P.S. Crozier, P.J. in't Veld, A. Kohlmeyer, S.G. Moore, T.D. Nguyen, LAMMPS-a flexible simulation tool for particle-based materials modeling at the atomic, meso, and continuum scales, Computer Physics Communications, 271 (2022) 108171.

[63] A. Stukowski, Visualization and analysis of atomistic simulation data with OVITO–the Open Visualization Tool, Modelling and simulation in materials science and engineering, 18 (2009) 015012.

[64] C.-F. Yen, Ballistic impact modeling of composite materials, in: Proceedings of the 7th international LS-DYNA users conference, 2002, pp. 15-23.

[65] F. Guo, Q.G. Fei, Y.B. Li, P.W. Zhang, M. Wang, J.W. Yu, Novel statistical analysis method for determining shear strength of C/C composite pin, Ceramics International, 46 (2020) 5262-5270.

[66] M. Tehrani, A.Y. Boroujeni, T.B. Hartman, T.P. Haugh, S.W. Case, M.S. Al-Haik, Mechanical characterization and impact damage assessment of a woven carbon fiber reinforced carbon nanotube-epoxy composite, Composites Science and Technology, 75 (2013) 42-48.

[67] B.X. Bie, J.H. Han, L. Lu, X.M. Zhou, M.L. Qi, Z. Zhang, S.N. Luo, Dynamic fracture of carbon nanotube/epoxy composites under high strain-rate loading, Compos Part a-Appl S, 68 (2015) 282-288.

[68] H. Ming-Yuan, J.W. Hutchinson, Crack deflection at an interface between dissimilar elastic materials, International journal of solids and structures, 25 (1989) 1053-1067.

[69] Y. Cao, W. Shen, N. Burlion, J.-F. Shao, Effects of inclusions and pores on plastic and viscoplastic deformation of rock-like materials, International Journal of Plasticity, 108 (2018) 107-124.

[70] S. Dietrich, J.-M. Gebert, G. Stasiuk, A. Wanner, K.A. Weidenmann, O. Deutschmann, I. Tsukrov, R. Piat, Microstructure characterization of CVI-densified carbon/carbon composites with various fiber distributions, Composites science and technology, 72 (2012) 1892-1900.

[71] Y. Liu, Q. Fu, F. Zhao, G. Sun, H. Li, Internal friction vs. thermal shock in C/C composites, Composites Part B: Engineering, 106 (2016) 59-65.